Grinding Wheel Motion and Force Analysis in Atherosclerotic Plaque Removal by Atherectomy

by

Yihao Zheng

A dissertation submitted in partial fulfillment
of the requirements for the degree of
Doctor of Philosophy
(Mechanical Engineering)
in The University of Michigan
2016

Doctoral Committee:

Professor Albert J. Shih, Chair
Professor Joseph L. Bull
Professor Hitinder S. Gurm
Assistant Professor Chinedum E. Okwudire
Professor Kazuhiro Saitou

To my family

ACKNOWLEDGMENTS

I am truly grateful for the countless support provided by many people along the way to my degree.

First of all, I would like to express my most sincere gratitude to my advisor, Professor Albert Shih, for his endless patience, guidance, and support. I have learned from him in any possible aspect: conducting research, writing paper, giving presentation, supervising students, teaching, networking, loving family, and keeping exercise. Most importantly, he redefined the word "diligence" in my vocabulary. He, being the most hardworking man I have ever known, has been inspiring me to always carry passion and perseverance with me.

My deepest gratitude also goes to my committee members. I really appreciate Professor Joseph Bull for his valuable suggestions on the fluid dynamics modeling and generous support with the particle imaging velocimetry equipment. I feel so lucky to know Doctor Hitinder Gurm who has been providing his clinical insights in my research and encouragement on my career. I would like to thank Professor Chinedum Okwudire for his kind support and inspiration as a role model for young faculties. I truly appreciate Professor Kazuhiro Saitou for passing me the philosophy in modeling and guiding me on scientific research method.

I would like to thank Yang Liu and Yao Liu who have been working with me and helped me out when I was in need. Special thanks go to John Pitre for his help on tuning PIV experimental setup and Luis Savastano for providing specimen for testing and exciting research ideas. I would also like to thank all my current and former lab mates working in WuMRC, especially Bruce Tai, Roland Chen, Yancheng Wang, and Barry Belmont for their suggestions and help. I have been enjoying my life here very much because of my

dearest friends: Weiyu, Molong, Zhenyu, Weisi, Xun, Wubing, Huanyi, and Yan. They are all genuinely good people. I feel really lucky to meet them in my life.

This thesis would not have been possible without the help of many people from across and outside the university, including Malcolm Miranda from the college of engineering high-performance computing support, Bobby Kerns from the Michigan center for materials characterization, Pilar Herrera-Fierro from the Lurie nanofabrication lab, Professor Barney Klamecki from the University of Minnesota, and Rob Kholer from the Cardiovascular Systems Inc.

Last but not the least, I want to say, I love you, to my parents and Luzi. Their love and trust mean the world to me.

TABLE OF CONTENTS

LIST OF FIGURES

LIST OF TABLES

ABSTRACT

Atherectomy is a catheter-based interventional procedure to remove the atherosclerotic plaque off the arterial wall to restore the blood flow and treat cardiovascular diseases. During atherectomy, a metal bond diamond grinding wheel driven by a long flexible drive shaft is inserted into patient's artery and rotates up to 230,000 rpm to pulverize the plaque into fine debris absorbable by blood and vessels. The grinding wheel motion inside the artery and the grinding force applied on the lesion are poorly understood though critical to the procedure complications including dissection (breakage of the vessel), restenosis (regrowth of the plaque), vasospasm (sudden constriction of the vessel), and slow-flow / no-reflow (downstream embolism caused by oversized debris).

This dissertation studies the grinding wheel motion and the associated blood hydraulic force and plaque grinding force during atherectomy. First, an experiment utilizing a transparent tissue-mimicking artery phantom, a high-speed camera, and a piezoelectric dynamometer was conducted to visualize the grinding wheel motion and measure the force on the artery phantom. Second, a computational fluid dynamics model was established to understand the blood flow field near the grinding wheel and the hydraulic force and validated by the particle imaging velocimetry. Third, a grinding force model was built based on the Hertz contact and the smoothed particle hydrodynamics simulation to describe the impact and cutting forces on the plaque and experimentally validated.

The grinding wheel orbits around the vessel lumen in the direction of its rotation. The orbital speed increases with the rotational speed and the size of the grinding wheel. The grinding wheel orbits at the orbital speed of 8,832, 9,210, 9,618, 9,930, and 10,248 rpm in a 4 mm lumen and 4,452, 4,638, 4,836, 5,052, and 5,262 rpm in the 6 mm lumen, while rotating at 135,000, 145,000, 155,000, 165,000, and 175,000 rpm, respectively, when

a 2.38 mm burr is tested in a PVC arterial phantom. This orbital motion is caused by the rotation-induced blood flow. The hydraulic force on the grinding wheel during orbiting is small comparing to the grinding force. The grinding force is 1.84, 1.92, and 2.22 N at 135,000, 155,000, and 175,000 rpm rotational speed, respectively, when a 2.38 mm diameter burr is tested in a bovine bone sample with a 4 mm lumen. While orbiting around the lumen, the grinding wheel bounces on the wall of the plaque, leaving discrete grinding marks. The bouncing grinding wheel impact force is the dominant component of the grinding force and the cutting component for plaque removal is relatively small.

These findings facilitate to improve the atherectomy clinical guidelines and the device design. A grinding wheel smaller than the lesion lumen can remove the plaque due to its orbital motion, and the traditional clinical technique of increasing the grinding wheel size for removing more plaque may not be necessary. To reduce the atherectomy grinding force, lower rotational speed and smaller grinding wheel size and mass are suggested. Utilizing the grinding wheel orbital motion, new device can be designed to restore the patency of small, tortuous, and delicate luminal structures.

CHAPTER 1
INTRODUCTION

1.1 Motivation

Ischemic heart disease, the number one cause of death in the world [1], is caused by atherosclerotic plaque building-up within a coronary artery. Similarly, the plaque blockage in peripheral arteries leads to peripheral artery occlusive disease. Currently in the US, there are 16.3 million [2] and 18 million [3] patients suffering from ischemic heart and peripheral artery occlusive diseases, respectively. The root-cause of each of these diseases is atherosclerosis, the accumulation of fatty and calcified materials, also known as plaque, on the arterial wall. As it develops, atherosclerosis results in narrowing and hardening of the artery, restricting blood flow.

Angioplasty is a standard treatment of these cardiovascular diseases to open the plaque blockage by inflating a balloon inside the narrowed section and compressing the plaque against the vessel wall. A stent is usually placed during angioplasty to keep the artery open. In the US, about 600,000 angioplasty procedures are performed every year [4]. However, angioplasty ballooning and stenting are difficult in severely hardened lesions due to plaque calcification, bifurcation, ostial stenosis, and in-stent restenosis [5]. In these situations, atherectomy is often required to remove the plaque.

Atherectomy, an interventional cardiology procedure, removes the calcified plaque from the vessel wall, via a specialized catheter equipped with a grinding wheel, cutting blade, or laser filament. Grinding-based atherectomy, pulverizing the plaque into fine debris absorbable by the blood and vessel, is the most widely used atherectomy procedure.

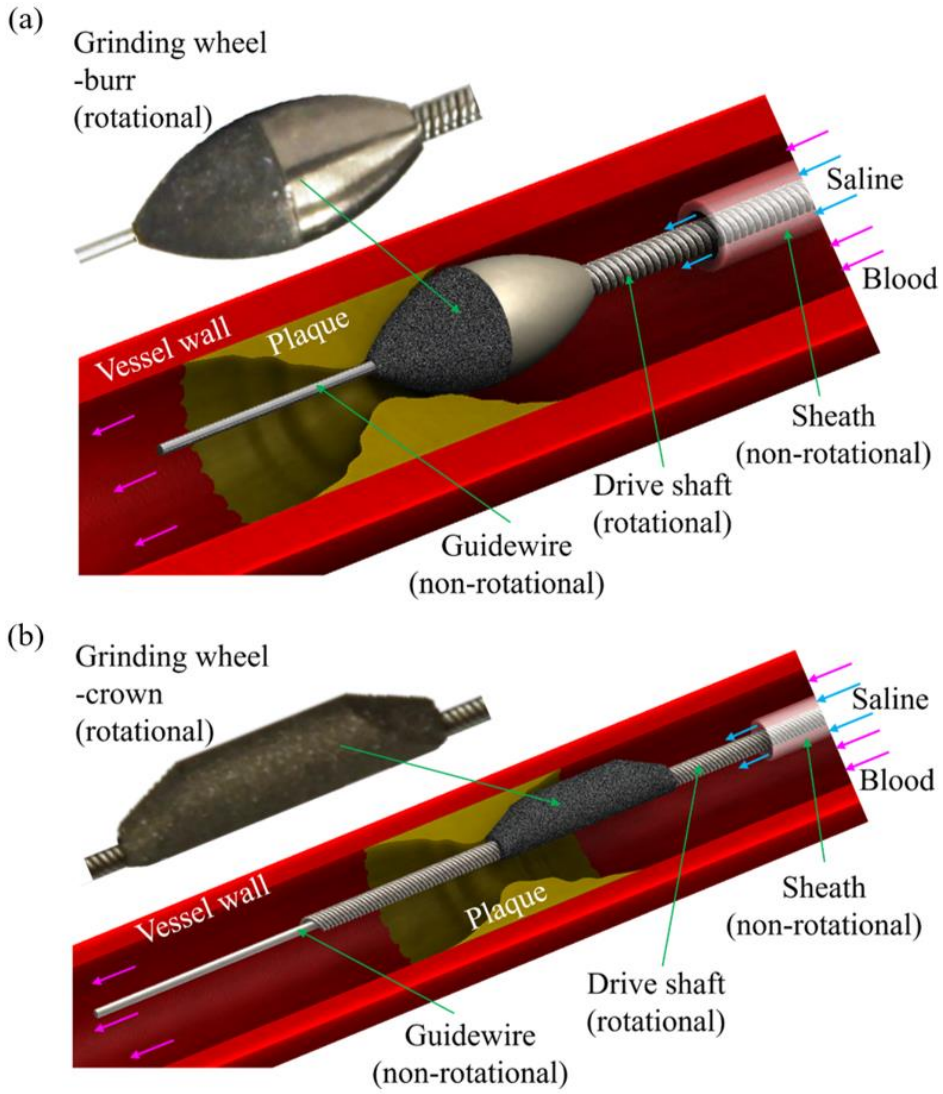

Figure 1.1 Grinding-based atherectomy devices: (a) Rotablator™ rotational atherectomy and (b) Diamondback 360® orbital atherectomy.

Rotablator™ rotational atherectomy by Boston Scientific (Natick, MA) and Diamondback 360® orbital atherectomy by Cardiovascular System Inc. (Saint Paul, MN) are two common grinding-based atherectomy devices. These two devices, as shown in Figure 1.1, share a similar mechanism of action. A high-speed rotating grinding wheel, driven by a flexible drive shaft, translates along a non-rotational guidewire through the lesion to sand the plaque. The rotating drive shaft is contained in a non-rotational plastic sheath where saline is infused to provide cooling and lubrication. Blood flows outside the sheath and carries the debris into the human circulation system. Grinding wheel geometry is the major difference between these two devices: an axisymmetric prolate spheroid with

half abrasive coating in rotational atherectomy (Figure 1.1(a)) and a wedged cylinder off-centered mounted on the drive shaft in orbital atherectomy (Figure 1.1(b)). Clinically, the grinding wheels are commonly known as burr and crown for rotational and orbital atherectomy, respectively.

Atherectomy has been extensively investigated in clinical studies but the complication rates are still high. Table 1.1 summarized the major complication rates reported in five key coronary atherectomy clinical trials. Major adverse cardiovascular events include death, myocardial infarction (MI), and target lesion/vessel revascularization (TLR/TVR). Additionally, angiographic complications (dissection, perforation, acute closure, and side branch loss), slow-flow/no-reflow, vasospasm, and burr entrapment were observed.

Table 1.1 Major complication rates in key coronary atherectomy clinical trials.

Trial	Patient Number	Death %	MI (Q + Non-Q wave) %	In-Hospital TLR/TVR %	Follow-up TLR/TVR % (months)
COBRA [6]	252	0.4	- (2.4 + -)	-/-	-/23 (6)
DART [7]	227	0.4	2.2 (0 + 2.2)	4.0/0.9	25/3.5 (12)
ROTAXUS [8]	240	1.7	1.7 (- + -)	-/0.8	11.7/- (9)
ORBIT II [9]	443	0.2	9.3 (0.7 + 8.6)	0.7/0.7	4.7/1.9 (12)
ROTALINK I [10]	1397	0.8	3.6 (- + -)	0.4/-	11.7/- (28)

Associated with this high complication rate, is a lack of consensus in atherectomy techniques, including selection of the grinding wheel size and rotational speed. In rotational atherectomy, Tomey *et al*. [11] found the use of a single burr with the burr-to-artery diameter ratio of 0.5 to 0.6 to be optimal, while Barbato *et al*. [12] suggested using multiple burrs by stepping up the size from 1.25 to 1.5 and then to 1.75 mm. Some clinical studies [11,13-15] suggested that 140,000-160,000 rpm is the optimum burr rotational

speed. An European review study [12] recommended a wider speed range, 135,000-180,000 rpm. However, a few later clinical studies utilized rotational speeds over 200,000 rpm [16-18].

Surprisingly, atherectomy has been seldom studied from the engineering perspective. Reisman *et al.* [19,20] experimentally related rotational speed to the degree of platelet aggregation and thermal injury. Lovik *et al.* [21] assessed tissue thermal damage with a finite element simulation model with experimental validation. Nakao *et al.* [22] and Lee *et al.* [23] focused on the surface pattern of the grinding wheel, without considering the compliance of the tissue. Ramazani-Rend *et al.* [24] numerically and experimentally proved the absence of cavitation in orbital atherectomy. Helgeson *et al*. [25] investigated the plaque debris trajectory and agglomeration within the blood. Adams *et al.* [26] and Kohler *et al.* [27] experimentally examined the particle size and analyzed grinding tool dynamics without the arterial wall interaction.

The grinding wheel motion inside the artery and the grinding force applied on the lesion are poorly understood though critical to atherectomy complications including dissection (breakage of the vessel), restenosis (regrowth of the plaque), vasospasm (sudden constriction of the blood vessel), and slow-flow / no-reflow (downstream embolism caused by oversized debris) [11,12].

1.2 Research Goal and Objectives

The goal of this research is to understand the grinding wheel motion and associated grinding and blood hydraulic forces in plaque removal by atherectomy. To achieve this goal, three objectives are identified:

(1) Experimentally visualize the grinding wheel motion in a tissue-mimicking artery phantom and measure the force experienced by the phantom during atherectomy.

(2) Develop a computational fluid dynamics model to understand the flow field near the rotating grinding wheel, validate this model by particle imaging

velocimetry experiment, and estimate the hydraulic force on the grinding wheel with this model.

(3) Establish a grinding force model to describe the grinding wheel interaction with the plaque, validate this model by experimental measurement, and simulate the plaque grinding process by multi-grain smoothed particle hydrodynamics modeling.

Achieving these objectives will provide engineering insights in the atherectomy mechanism of action to the clinicians and device manufacturers for improving the procedure guidelines and the device design.

1.3 Organization of the Dissertation

The rest of this dissertation is organized as follows:

Chapter 2 presents an experimental investigation of the grinding wheel motion and force in atherectomy. The experimental setup with a tissue-mimicking artery phantom, a high-speed camera, and a piezoelectric dynamometer is introduced. An orbital motion of the grinding wheel is observed.

Chapter 3 investigates the flow field associated with the orbital motion of the rotating grinding wheel. A computational fluid dynamics model validated by particle imaging velocimetry is presented.

Chapter 4 introduces a discrete grinding mechanism with a bouncing grinding wheel. The calculation of the impact force by Hertz contact model and the cutting force simulation by multi-grain smoothed particle hydrodynamics are elaborated. The modeled grinding force is compared with measurement.

Chapter 5 draws the conclusions and summarizes the original contributions of the dissertation. Several topics for future research are also proposed.

References

[1] World Health Organization. Global atlas on cardiovascular disease prevention and control. 2011. 194 p.

[2] Roger VL, Go AS, Lloyd-Jones DM, Benjamin EJ, Berry JD, Borden WB, *et al.* Heart disease and stroke statistics--2012 update: a report from the American Heart Association. Circulation. 2012;125(1):e2-e220.

[3] Schiavetta A, Maione C, Botti C, Marino G, Lillo S, Garrone A, *et al.* A phase II trial of autologous transplantation of bone marrow stem cells for critical limb ischemia: results of the Naples and Pietra Ligure evaluation of Stem Cells study. Stem Cells Transl Med. 2012;1(7):572-8.

[4] Fang G, Ai W, Leeflang S, Duszczyk J,Zhou J. Multipass cold drawing of magnesium alloy minitubes for biodegradable vascular stents. Mater Sci Eng C Mater Biol Appl. 2013;33(6):3481-8.

[5] Fitzgerald P, Ports T, Yock P. Contribution of localized calcium deposits to dissections after angioplasty. Circulation. 1992; 86(1): 64-70.

[6] Dietz U, Rupprecht HJ, Ekinci O, Dill T, Erbel R, Kuck KH, *et al*. Angiographic analysis of immediate and long-term results of PTCR vs. PTCA in complex lesions (COBRA study). Catheter Cardiovasc. Interv. 2001;53:359-67.

[7] Mauri L, Reisman M, Buchbinder M, Popma JJ, Sharma SK, Cutlip DE, *et al*. Comparison of rotational atherectomy with conventional balloon angioplasty in the prevention of restenosis of small coronary arteries: results of the dilatation vs ablation revascularization trial targeting restenosis (DART). American Hearth Journal. 2003;145:847-54.

[8] Abdel-Wahab M, Richardt G, Joachim Büttner H, Toelg R, Geist V, Meinertz T, *et al*. High-speed rotational atherectomy before paclitaxel-eluting stent implantation in complex calcified coronary lesions: the randomized ROTAXUS (Rotational Atherectomy Prior to Taxus Stent Treatment for Complex Native Coronary Artery Disease) trial. JACC Cardiovasc Interv. 2013;6(1):10-9.

[9] Chambers JW, Feldman RL, Himmelstein SI, Bhatheja R, Villa AE, Strickman NE, *et al*. Pivotal trial to evaluate the safety and efficacy of the orbital atherectomy system

in treating de novo, severely calcified coronary lesions (ORBIT II). JACC Cardiovasc Interv. 2014;7(5):510-8.

[10] Cortese B, Aranzulla TC, Godino C, Chizzola G, Zavalloni D, Tavasci E, *et al*. Drug-eluting stent use after coronary atherectomy: results from a multicentre experience - The ROTALINK I study. J Cardiovasc Med. 2016;17(9):665-72.

[11] Tomey MI, Kini AS, Sharma SK. Current status of rotational atherectomy. JACC Cardiovasc Interv. 2014;7(4):345-53.

[12] Barbato E, Carrié D, Dardas P, Fajadet J, Gaul G, Haude M *et al*. European expert consensus on rotational atherectomy. EuroIntervention. 2015;11(1):30-6.

[13] Zimarino M, Corcos T, Bramucci E, Tamburino C. Rotational atherectomy: a "survivor" in the drug-eluting stent era. Cardiovasc Revasc Med. 2012;13(3):185-92.

[14] Mota P, de Belder A, Leitão-Marques A. Rotational atherectomy: Technical update. Rev Port Cardiol. 2015;34(4):271-8.

[15] Tomey MI, Sharma SK. Interventional options for coronary artery calcification. Curr Cardiol Rep. 2016;18(2):12.

[16] Maejima N, Hibi K, Saka K, Akiyama E, Konishi M, Endo M, *et al*. Relationship between thickness of calcium on optical coherence tomography and crack formation after balloon dilatation in calcified plaque requiring rotational atherectomy. Circ J. 2016;80(6):1413-9.

[17] Kawata M, Kato Y, Takada H, Kamemura K, Matsuura A, Sakamoto S. Successful rotational atherectomy for a repetitive restenosis lesion with underexpansion of double layer drug-eluting stents due to heavily calcified plaque. Cardiovasc Interv Ther. 2016;31(1):65-9.

[18] Jinnouchi H, Kuramitsu S, Shinozaki T, Kobayashi Y, Hiromasa T, Morinaga T, *et al*. Two-year clinical outcomes of newer-generation drug-eluting stent implantation following rotational atherectomy for heavily calcified lesions. Circ J. 2015;79(9):1938-43.

[19] Reisman M, Shuman BJ, Dillar D, Fei R, Misser KH, Gordon LS, Harms V. Analysis of low-speed rotational atherectomy for the reduction of platelet aggregation. Cathet Cardiovasc Diagn. 1998;45(2):208-14.

[20] Reisman M, Shuman BJ, Harms V. Analysis of heat generation during rotational atherectomy using different operational techniques. Cathet Cardiovasc Diagn. 1998;44(4):453-5.

[21] Lovik RD, Abraham JP, Sparrow EM. Assessment of possible thermal damage of tissue due to atherectomy by means of a mechanical debulking device. In: the 10th ASME Summer Bioengineering Conference (SBC2008); Marco Island, FL. 2008; p.799-800.

[22] Nakao M, Tsuchiya K, Maeda W, Iijima D. A rotating cutting tool to remove hard cemented deposits in heart blood vessels without damaging soft vessel walls. CIRP Ann-Manuf Techn. 2005;54(1):37-40.

[23] Lee G, Wie K, Hong Y, Yoon H, Kim M, Kim H, Ahn S. A study of tool pattern design for calcified-atherosclerotic-plaque removal robot. In: the 3rd IEEE RAS & EMBS International Conference on Biomedical Robotics and Biomechatronics; Tokyo, Japan. 2010; p.582-7.

[24] Ramazani-Rend R, Chelikani S, Sparrow EM and Abraham JP. Experimental and numerical investigation of orbital atherectomy: absence of cavitation. J Biomed Sci Eng. 2010;3(11):1108-16.

[25] Helgeson ZL, Jenkins JS, Abraham JP, Sparrow EM. Particle trajectories and agglomeration/accumulation in branching arteries subjected to orbital atherectomy. Open Biomed Eng J. 2011;5:25-38.

[26] Adams GL, Khanna PK, Staniloae CS, Abraham JP, Sparrow EM. Optimal techniques with the Diamondback 360° system achieve effective results for the treatment of peripheral arterial disease. J Cardiovasc Transl Res. 2011;4(2):220-9.

[27] Kohler R, Nguyen T, McBroom J. Removal of calcified plaque utilizing orbital atherectomy. In: the ASME 2014 International Manufacturing Science and Engineering Conference; Detroit, MI. 2014; p.V002T02A032.

CHAPTER 2
EXPERIMENTAL INVESTIGATION OF THE GRINDING WHEEL DYNAMICS IN ATHERECTOMY

2.1 Introduction

Missing from the review of engineering studies listed in Section 1.1, are descriptions, qualitative or quantitative, of the grinding wheel motion and contact forces with lesions in orbital atherectomy associated with the procedure safety, efficacy (vessel lumen enlargement and tissue softening), and complications such as dissection and spasm.

This chapter seeks to address this dearth by experimentally investigating the motion and contact forces of the crown in orbital atherectomy. A high-speed camera and image processing technique were utilized to visualize and quantify the crown motion and its interaction with the wall of a transparent arterial phantom made of tissue-mimicking polyvinyl chloride (PVC). Forces were measured simultaneously by a piezoelectric force dynamometer with sufficient sensitivity and bandwidth for such rapid dynamic measurements.

Within the body of this chapter, the experimental setup and image processing techniques are first introduced, the measured results of the crown motion and contact forces are then presented, and finally the agreement between the observed crown motion and contact forces as well as a similar orbital motion observed in rotational atherectomy is discussed.

2.2 Materials and Methods

2.2.1 Experimental setup

The experimental setup, as shown in Figure 2.1, consisted of three modules – the atherectomy device, an arterial phantom, and the measurement system – discussed in the following sections.

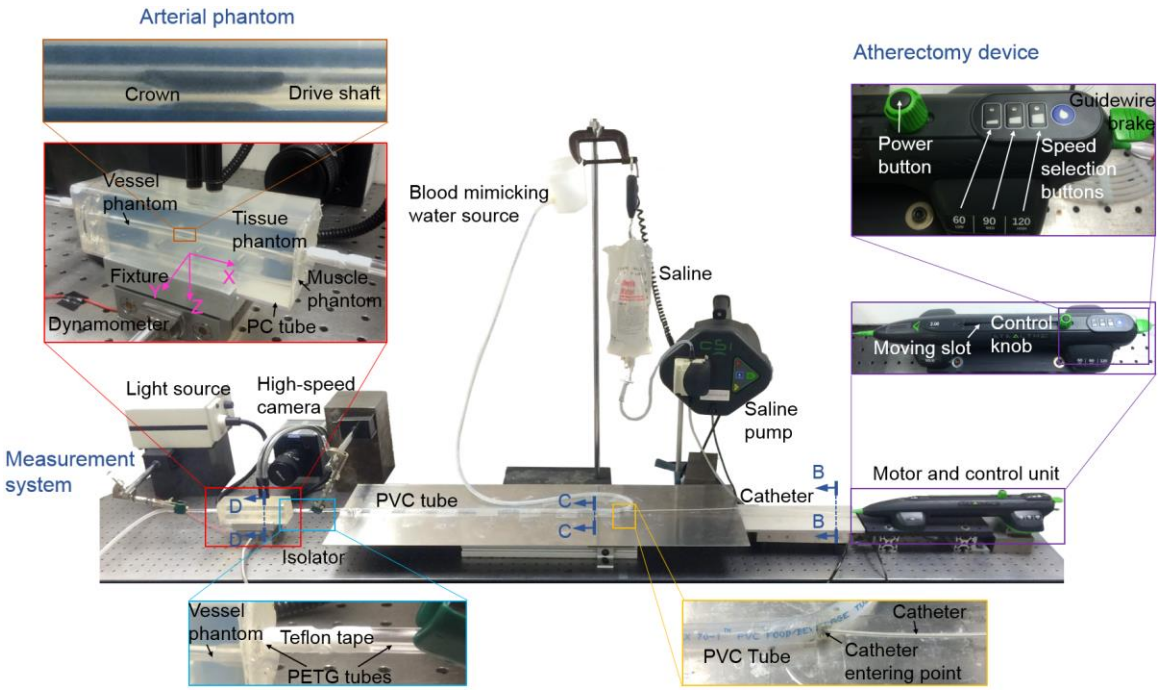

Figure 2.1 Experimental setup for orbital atherectomy.

2.2.1.1 Atherectomy device

The orbital atherectomy device used in this study was the Diamondback 360® (2 mm solid crown) by Cardiovascular Systems Inc. (St. Paul, MN). This device consists of three units: (1) a motor and control unit, (2) a catheter, and (3) saline and a saline pump.

The motor and control unit (Figure 2.1) includes an electric motor, a control knob to axially move the catheter, and a set of speed selection buttons to generate three rotational speeds: 60,000, 90,000 and 120,000 rpm.

The catheter, as illustrated in Figure 1.1(b), is the part inserted into a patient's vessel during atherectomy. The catheter (whose detailed construction is shown in Figure 2.2)

consists of a guidewire, an abrasive crown, a drive shaft, and a sheath. A cross-sectional view of the catheter (marked as B-B in Figures 2.1 and 2.2(a)) is shown in Figure 2.2(b). A guidewire (0.36 mm diameter, stainless steel) extends from the motor through the drive shaft and crown to beyond the plaque (Figure 1.1(b)). During atherectomy, one end of the guidewire is located distal to device across the plaque with the other end fixed by a brake in the motor and control unit (Figure 2.1). Around the guidewire is a 1,640 mm long drive shaft, made of six 0.15 mm diameter coils helically wound with a 0.79 mm outer diameter

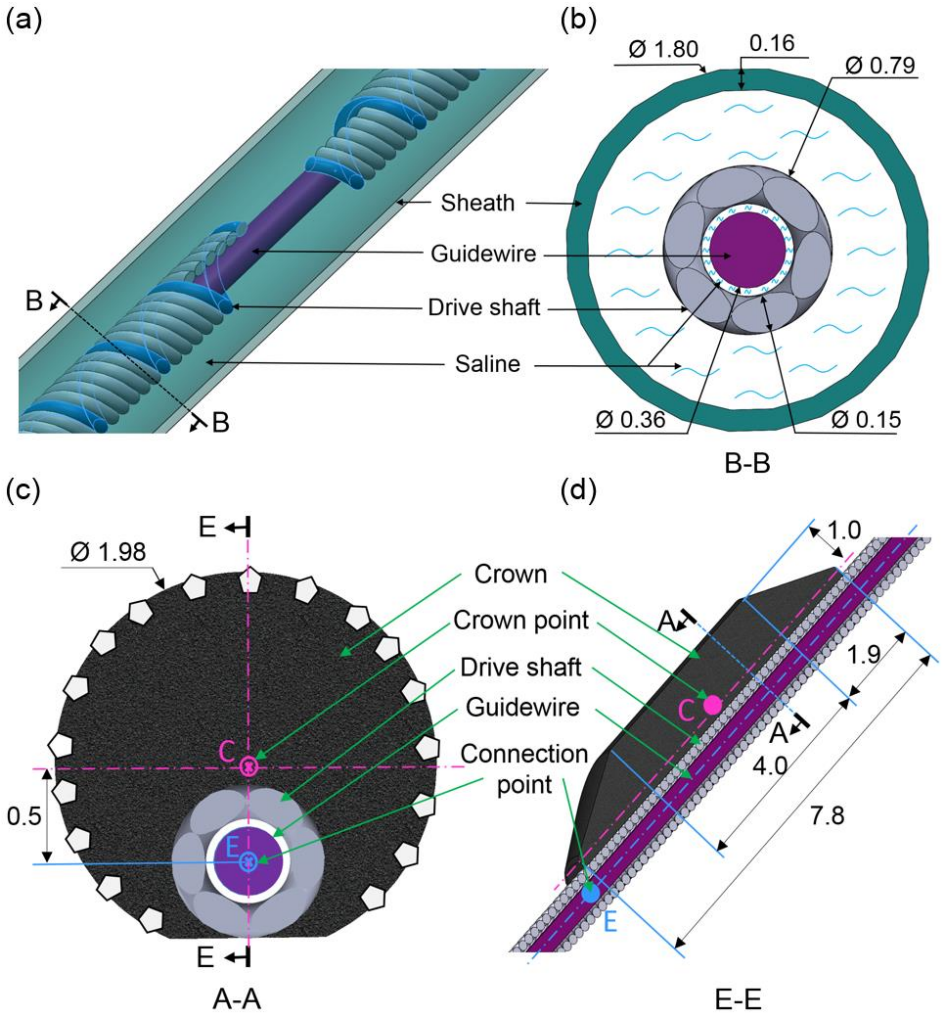

Figure 2.2 Catheter: (a) the guidewire, drive shaft and sheath, (b) cross-section B-B, (c) crown cross-section A-A, and (d) cross-section E-E. (unit: mm)

(OD), as shown in Figures 2.2(a) and (b). The drive shaft rotates about and moves along the guidewire. One side of the shaft connects to the motor. The other side is a free end as

shown in Figure 1.1(b). Joined on the drive shaft, the crown is 30 mm away from the free end of the shaft. The cross-sectional views A-A (Figure 2.2(c)) and E-E (Figure 2.2(d)) demonstrate the crown (a 1.98 mm OD and 7.8 mm long rod) which is wedged on both sides to reduce the stress concentration when in contact with the plaque. The crown, made of tungsten, has a layer of 0.03 mm average size diamond impregnated on the surface [7]. As seen in Figures 2.2(c)-(d), crown point, C, was defined as the middle of the cylindrical crown centerline, and connection point, E, one end of the crown on the guidewire axis where the drive shaft axially joins the crown and is offset by 0.5 mm from the crown centerline (Figure 2.2(c)). The sheath is a high-density polyethylene tube (1.8 mm OD and 0.16 mm wall thickness) and prevents direct contact between the high-speed rotating drive shaft and the vessel wall. Inside the sheath, saline, pumped via a roller pump at a flow rate of 45 ml min^{-1} to the treatment site, flows to provide lubrication and remove heat generated by the friction of the drive shaft between the guidewire and the sheath.

2.2.1.2 Arterial phantom

The arterial phantom meant to simulate the artery and the blood flow consisted of (1) a tissue-mimicking phantom, (2) a blood-mimicking water source, (3) a PVC tube connecting the phantom and water source, and (4) force isolators between the PVC tube and the tissue phantom.

The transparent tissue-mimicking phantom, as shown in Figures 2.3(a) and (b), consisted of a PVC vessel and muscle phantom and a square polycarbonate (PC) tube to encase the soft material. Its geometry was designed to mimic the human proximal popliteal artery region, one of the most common locations of lower extremity atherosclerosis [1]. To measure the force during the procedure, the outer square PC tube (50.8 mm outer width, 2.03 mm wall thickness, and 150 mm length) was mounted to a piezoelectric dynamometer (Model 9256-C by Kistler) via a custom fixture (Figure 2.1). Inside the tube were the PVC vessel and muscle phantoms. The vessel phantom, to accommodate the proximal popliteal artery's elastic properties [2] and anatomy [3], was made of soft PVC (45 kPa elastic modulus) and had a 4.8 mm inner diameter (ID) and a 2.0 mm wall thickness. The muscle phantom surrounded the vessel phantom and bounded by the outer PC tube was made of

PVC with a lower elastic modulus (about 8 kPa). The mechanical properties and fabrication of this tissue mimicking PVC were introduced by Li *et al.* [4]

To fabricate the tubular vessel phantom, a 4.76 mm diameter aluminum rod was dipped into PVC plastisol (M-F Manufacturing Co., Fort Worth, TX) heated to 150°C for 20 min and degassed in a vacuum chamber at –90 kPa for 10 min. To make the muscle phantom, the PVC plastisol was mixed in a 1:1 ratio with the plastic softener (M-F Manufacturing Co., Fort Worth, TX) and poured into the space between the vessel phantom (supported by the aluminum rod) and the square encasing tube. After the PVC was cooled to room temperature and cured, the aluminum rod was removed. The inner diameter of the vessel phantom became 4.8 mm after cooling as a result of the PVC shrinkage.

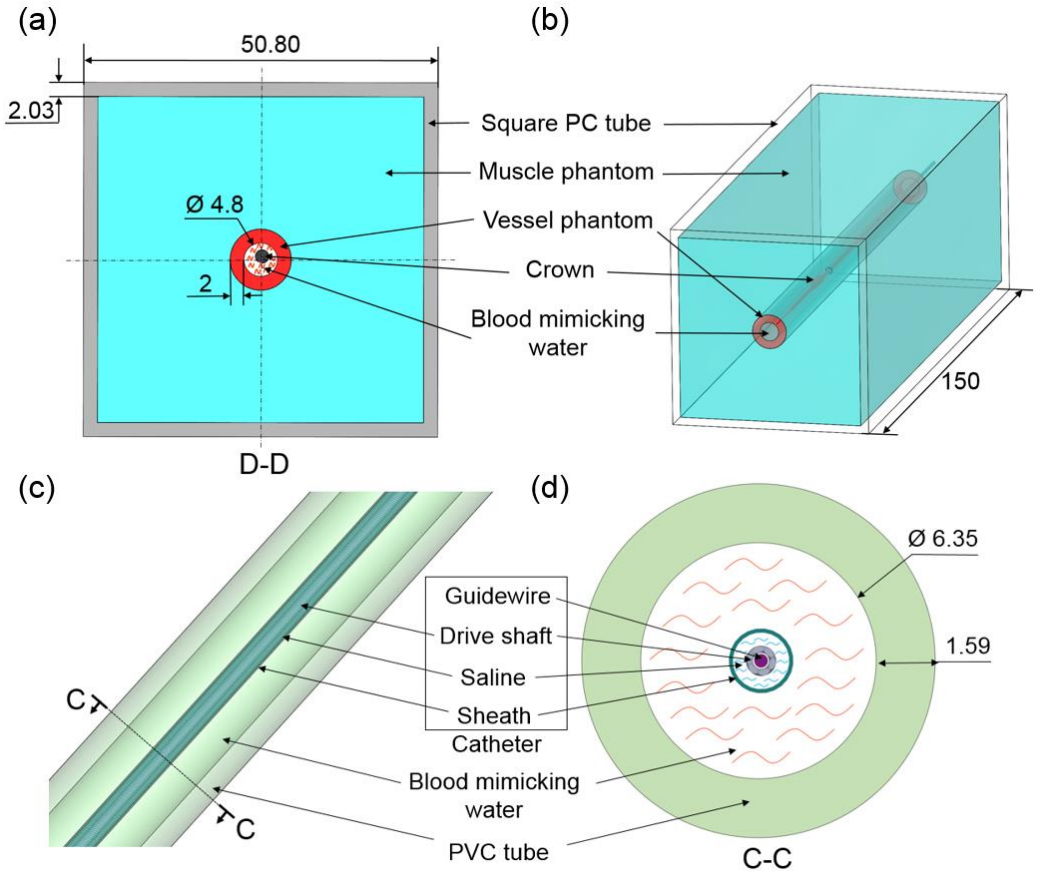

Figure 2.3 Arterial phantom: (a) tissue phantom cross-section D-D, (b) tissue phantom assembly with catheter inside, (c) horizontal section of the PVC tube with catheter inside, and (d) cross-section C-C. (unit: mm)

The blood mimicking water source was raised 1 m above the rest of the experimental setup, as shown in Figure 2.1, to force the water to flow through the PVC tube and the tissue phantom at a flow rate of 1.3 L min^{-1}. The PVC tube (ID of 6.35 mm, wall thickness of 1.59 mm, and 1.7 m in length) had a 0.7 m long horizontal section in the X direction connected to the tissue phantom and a vertical section in the Z direction connected to the blood mimicking water source. A 1.5 mm diameter hole was drilled into the PVC tube to allow the catheter to enter the horizontal section and access the tissue phantom. Figure 2.3(c) shows the catheter (1.8 mm OD) inside the PVC tube. The cross-section C-C of the PVC tube and catheter from Figure 2.3(c) is shown in Figure 2.3(d).

Force isolators were implemented on both sides of the tissue phantom to isolate the forces on the PVC tube induced by the vibration of the catheter. The isolators were individually made of two round polyethylene terephthalate (PETG) tubes (7.94 mm OD and 4.76 mm ID) connected with a 5 mm clearance by wrapping the Teflon tape.

2.2.1.3 Measurement system

Two key devices were used in this study to measure the crown dynamics: a high speed camera (Model FASTCAM-1024PCI by Photron) and a force dynamometer (both can be seen in the Figure 2.1). The camera was used to image the crown (through the transparent phantom) from the side or the front to record the crown motion. Recording at 18,000 frames per second (fps) allowed a minimum of 9 frames to be captured for each revolution of the crown even at its highest rotational speed setting of 120,000 rpm. A fiber optic light source (Model 8375 by Fostec) was used to deliver a bright, concentrated light necessary for proper image quality. The dynamometer was mounted under the tissue phantom, and measured the force in the Y and Z directions (Figure 2.1) at a sampling rate of 5,000 Hz. The Y- and Z-axis natural frequencies of this dynamometer (5,500 and 5,600 Hz [5]) were well above 2,000 Hz, the frequency experienced at the 120,000 rpm crown rotational speed.

2.2.2 Image processing

The images in the videos were processed in MATLAB (R2014a by MathWorks) to analyze the crown motion. A technique utilizing multiple thresholds was applied to divide

the pixels into distinct regions based on the intensity. The sample image, shown in Figure 4(a), had its pixels segmented into four levels of intensity, as shown in Figure 2.4(b). The pixels with the highest intensity, marked in red, were the drive shaft and the crown, due to the focused illumination. Since this technique distinguished the drive shaft and crown according to their consistently higher intensity level relative to the surrounding phantom material, it was an effective means to track the crown, even as it moved slightly beyond the focal plane of the camera.

Connection and crown points, E and C defined in Figures 2.2(c) and (d), were detected for motion tracking. As shown in Figure 2.4(b), the pixel with high intensity on the drive shaft closest to the crown was E. The pixel in the middle bottom of the high intensity region of the crown was C. The number of pixels from the bottom edge of the image to E or C represented E's or C's position within the image and was measured for every frame. The fast Fourier transform (FFT) was applied to identify peak frequencies in E and C motions.

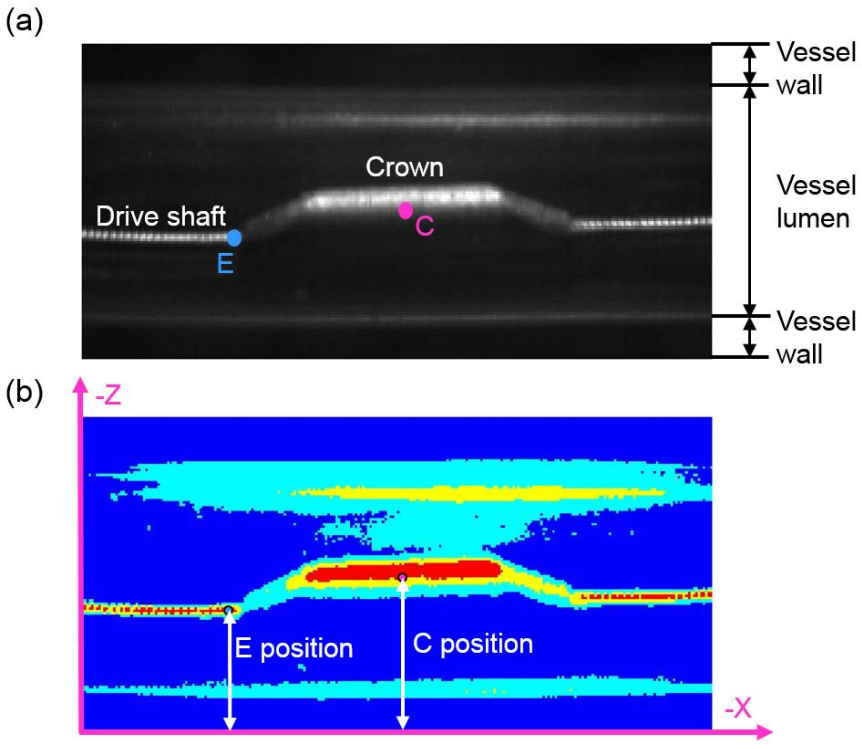

Figure 2.4 Image processing: (a) a sample image, (b) processed image with four levels of pixel intensity and point E and C positions.

2.2.3 Design of experiment

The crown motion in the vessel phantom was only axially restrained in X direction by locking the control knob during the tests. For each individual test, video and force data collection began 10 s after powering the device up and lasted for 5 s. Five tests were conducted for each crown rotational speed (60,000, 90,000, and 120,000 rpm). The mean and standard deviation (SD) of the results from each of these five repeated tests at the three rotational speeds are presented.

2.3 Results

The crown motion was found to be a combination of high-frequency rotation along the crown's axis and low-frequency orbiting around the vessel lumen. The measured forces confirmed these rotational and orbital frequencies observed in the crown motion. Results from the three crown rotational speeds (60,000, 90,000, and 120,000 rpm) are presented in Tables 2.1 and 2.2 and the analysis of the crown dynamics at 90,000 rpm is here illustrated as an example in Figures 2.5, 2.6, and 2.7.

2.3.1 Crown motion

Figure 2.5(a) shows the displacement of the connection point E in the Z direction for 23.3 ms at 90,000 rpm crown rotational speed. It is the superposition of a small-amplitude high-frequency motion upon a large-amplitude low-frequency motion (the data marked in this figure by a dashed line have been low-pass filtered at 50 Hz cutoff frequency). Honing in on a single high-frequency period from 11.1 to 11.8 ms, as shown in Figure 2.5(b), one can see via the video images of the crown at 9 time instances with a time step in between of 0.08 ms (Figure 2.5(c)) that the point E circled around the crown centerline, indicating the crown rotation.

The displacement of the crown point C in the Z direction over the same 23.3 ms time period is shown in Figure 2.5(d). The corresponding 9 images shown in Figure 2.5(e) have a time step of 2.9 ms and demonstrate the crown orbiting around the vessel lumen.

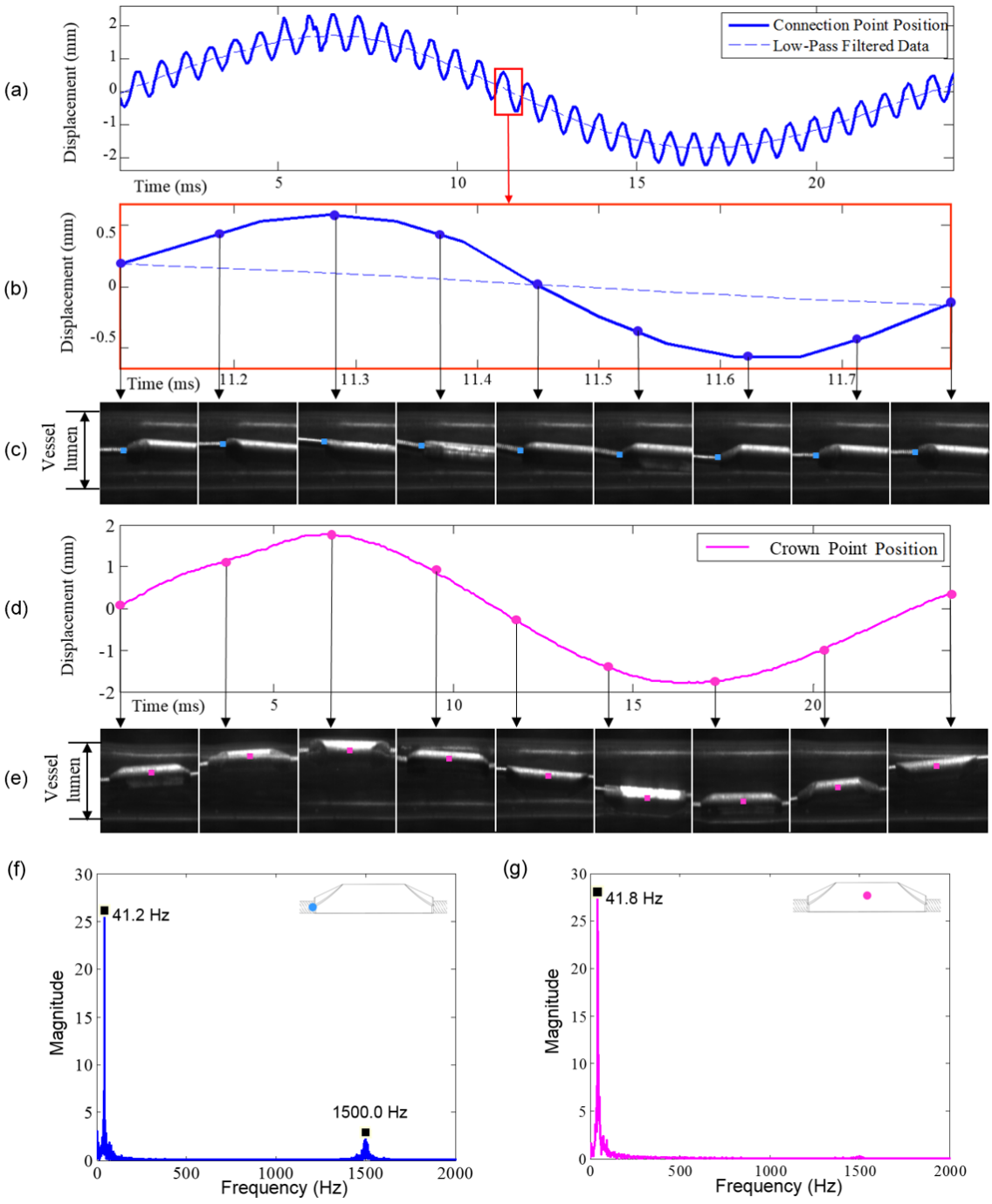

Figure 2.5 At 90,000 rpm crown rotational speed, the connection point E (a) measured motion, (b) zoom-in view of a high-frequency period, and (c) corresponding images; the crown point C (d) measured motion and (e) corresponding images; and motion frequency analysis of (f) E and (g) C.

This orbital motion explains the large-amplitude low-frequency component in the displacement of E (dash line in Figure 2.5(a)).

Frequency analysis results of the E and C displacement via FFT are shown in Figures 2.5(f) and (g), respectively. The high frequency in E motion (Figure 2.5(f)) was 1,500 Hz, corresponding to the 90,000 rpm rotational speed of the crown, and is the rotational frequency. The low frequency in E motion (Figure 2.5(f)) was 41.2 Hz, close to the crown orbital frequency (41.8 Hz peak frequency in Figure 2.5(g)).

The mean and SD of the rotational and orbital frequencies (obtained from the frequency analysis of the E and C displacement, respectively) of the crown motion in the five tests at three rotational speeds (60,000, 90,000, and 120,000 rpm) are summarized in the Table 2.1. Measured rotational frequencies of 1,003 and 1,500 Hz matched the rotational speed settings for 60,000 and 90,000 rpm, respectively. At 120,000 rpm, the instability of the crown rotational speed caused this value to range from 1,660 to 1,870 Hz (corresponding to 99,600 to 111,200 rpm) and is likely due to limitations of the driving motor. The crown orbital frequency in the vessel lumen for each rotational speed was 19.3, 38.2, and 40.5 Hz.

Table 2.1 Rotational (high) and orbital (low) frequencies in crown motion at three rotational speeds.

Rotational Speed (rpm)	Frequency	Mean (Hz)	SD (Hz)
60,000	Rotational (high)	1003.4	8.5
	Orbital (low)	19.3	0.6
90,000	Rotational	1499.6	3.0
	Orbital	38.2	1.7
120,000	Rotational	1660-1870	-
	Orbital	40.5	0.4

Figures 2.6(a) and (b) show the crown motion captured with the high-speed camera aimed along the vessel axis (X direction). Figure 2.6(a) traces a cycle of crown rotation in 0.72 ms when E (turquoise dot) completed one circle counterclockwise around C (magenta dot). The crown rotated about its cylindrical axis and moved smoothly (no high-frequency C motion in Figure 2.5(d)) against the vessel. Figure 2.6(b) demonstrates a cycle of the

crown orbiting to be about 24 ms with C traveling around the vessel lumen counterclockwise. The rotational and orbital directions of the crown were observed to be the same. To summarize the high speed camera observation of the crown rotation and orbiting, two schematic views are presented in Figures 2.6 (c) and (d).

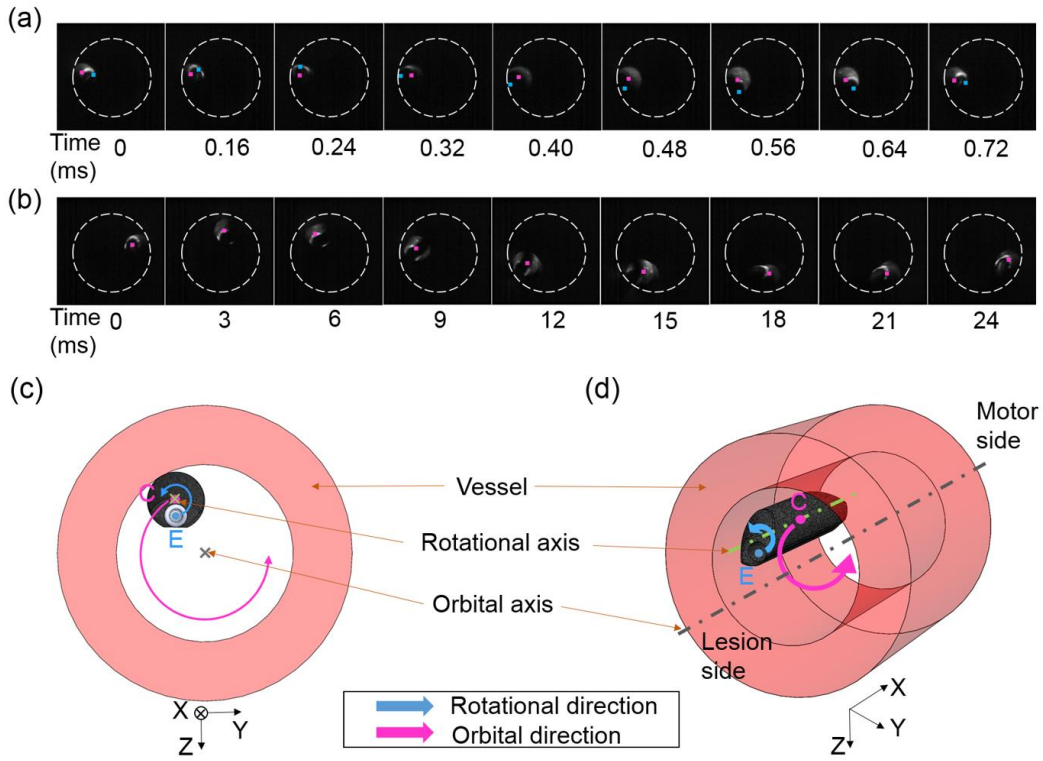

Figure 2.6 Crown rotation and orbiting: (a) one rotational cycle and (b) one orbital cycle observed by high-speed camera in axial direction when the crown rotates at 90,000 rpm (E in turquoise color, C in magenta color, and vessel lumen in circle), and (c) front and (d) perspective schematic views of the crown rotation and orbiting.

2.3.2 Contact force

Figure 2.7 shows the measured force in the Z- (F_Z) and Y-direction (F_Y) for one orbital period (24.4 ms) at the 90,000 rpm crown rotational speed. The combination of high and low frequencies was clearly seen in Figures 2.7(a) and (c). A low-pass filter (50 Hz cutoff) was applied, and the filtered data are shown in red dash line. The two dominant frequencies obtained from the FFT were 1,500 and 40.6 Hz for F_Z and 1,500 and 41.3 Hz for F_Y as shown in Figures 2.7(b) and (d), respectively. These two frequencies agree with

the image-based measurement of 1499.6 Hz rotational and 38.2 Hz orbital frequencies (seen in Table 2.1).

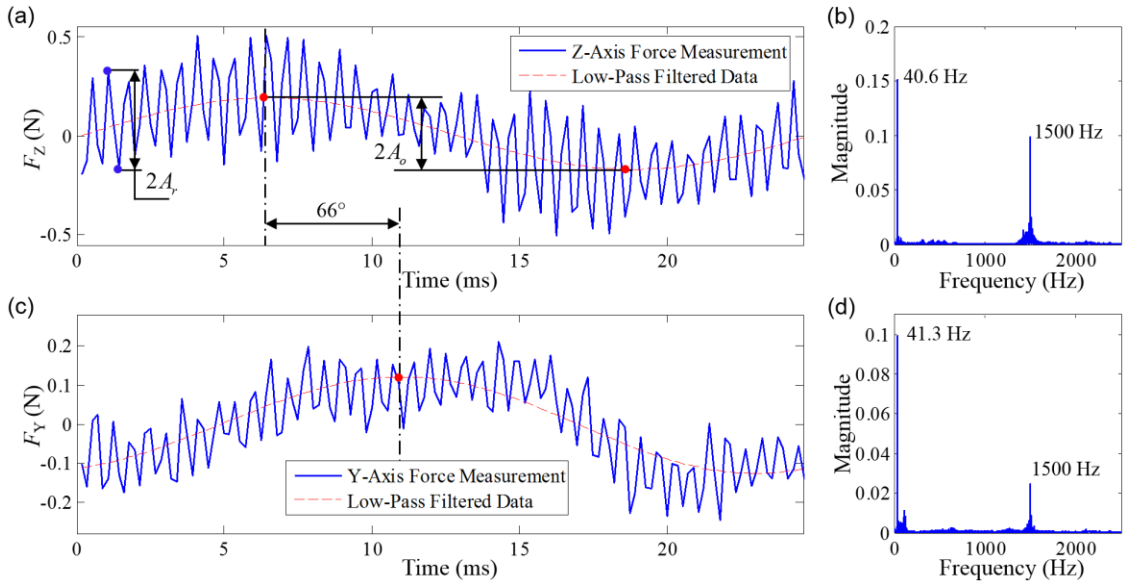

Figure 2.7 Force measurement at 90,000 rpm crown rotational speed: F_Z in the (a) time and (b) frequency domain; F_Y in the (c) time and (d) frequency domain.

The amplitudes of a representative rotational and orbital frequency period are marked as A_r and A_o, respectively, in Figure 2.7(a). The force F_Z can be represented as:

$$F_Z = A_r \sin(2\pi f_r t) + A_o \sin(2\pi f_o t) \tag{1.1}$$

where t is the time, f_r and f_o are the rotational and orbital frequencies, and A_r and A_o are the average amplitudes of the force components in the Z-direction in the rotational and orbital frequency, respectively. Adding A_r and A_o gives the average peak force, F_{peak}. The same analysis is repeated for F_Y. Table 2.2 summarizes the mean and SD of f_r, f_o, A_r, and A_o for the five repeated tests and F_{peak} at the three rotational speeds for F_Z and F_Y. The A_r and A_o were the highest at a rotation speed of 90,000 rpm, with the A_r and A_o at 120,000 rpm close to those at 90,000 rpm and higher than those of 60,000 rpm. The A_r and A_o in the Z-direction were found to be higher than those in the Y-direction, possibly due to the effects

of gravity and the dynamic response of the soft tissue phantom. More detailed study is required to understand the effect of crown rotational speed on A_r and A_o.

Table 2.2 Force measurement at three rotational speeds.

Rotational Speed (rpm)	Direc -tion	f_r (Hz) Mean (SD)	A_r (N) Mean (SD)	f_o (Hz) Mean (SD)	A_o (N) Mean (SD)	F_{peak} (N)
60,000	Z	1006.4 (12.4)	0.074 (0.001)	19.5 (0.9)	0.025 (0.002)	0.099
	Y	993.5 (4.3)	0.086 (0.009)	19.4 (1.0)	0.018 (0.001)	0.104
90,000	Z	1500.2 (0.4)	0.255 (0.014)	38.1 (1.3)	0.169 (0.010)	0.424
	Y	1500.2 (0.4)	0.111 (0.011)	38.3 (1.7)	0.100 (0.013)	0.211
120,000	Z	1637-1927	0.202 (0.007)	40.5 (0.4)	0.116 (0.007)	0.318
	Y	1645-1903	0.117 (0.002)	40.7 (0.3)	0.093 (0.002)	0.210

2.4 Discussions

Herein we have investigated crown motion and its contact force based on high-speed image capture and force measurement in a tissue-mimicking phantom. The crown motion and contact force consist of two dominant, rotational and orbital, frequencies.

2.4.1 Comparison of f_r and f_o measured based on image and force

At 60,000 and 90,000 rpm, the values of f_r in Tables 2.1 and 2.2 are very close. At 120,000 rpm, f_r varied within a similar range without a conclusive value for comparison. For f_o, the image-based measurements (19.3, 38.2, and 40.5 Hz in Table 2.1) were almost equal to those in Table 2.2 for F_Y (19.5, 38.1, and 40.5 Hz) and F_Z (19.4, 38.3, and 40.7 Hz) with less than 1% discrepancy, possibly as a result of the different sampling frequencies and the accompanying signal processing done for each method. The rotational frequency term exists due to the wedge shape of the crown (Figure 1.1(b)) leading to the varying contact area with the vessel during the crown rotation. The orbital frequency component results from the crown orbiting centrifugal force. As shown in Figure 2.8, a linear fit between $\ln(f_o)$ and $\ln(A_o)$ is observed with slope values of 2.41 and 2.34 and R-square values of 0.93 and 0.98 for F_Z and F_Y, respectively, at three rotational speeds,

confirming the quadratic relationship of the crown's orbital frequency to its the centrifugal force.

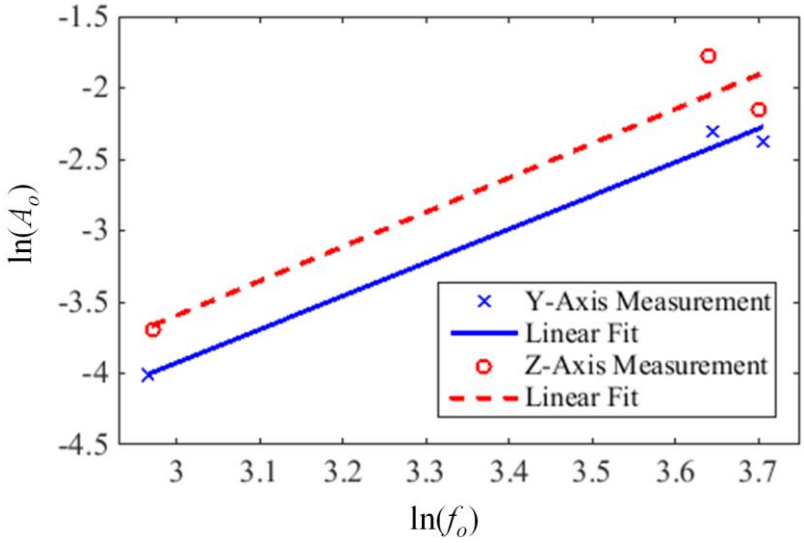

Figure 2.8 Linear fit between ln(f_o) and ln(A_o) for Y- and Z- axis measurement.

2.4.2 Heat dispersion and plaque stress softening

The crown orbital motion could reduce the heat accumulation and tissue thermal injury. Abrasive sanding is an energy intensive process and its accompanying heat, if accumulated, can cause blood coagulation and tissue thermal injury during atherectomy. The combination of rotational and orbital motions of the crown avoids any continuous contact between a specific region of the vessel and the rotating crown and allows continuous blood flow. Such characteristic behavior of the crown motion could be exploited to aid in heat dispersion making orbital atherectomy safe with respect to thermal necrosis of the artery wall [6].

Cyclic loading on the vessel in orbital atherectomy could soften the plaque tissue. Several studies [7-10] have demonstrated the stress softening of atherosclerotic plaque, similar to the Mullins effect in rubber [11]. In orbital atherectomy, the plaque undergoes cyclic loading due to the crown's orbital motion. The crown rotational motion contributes additional cyclic loading, elevating the local stress and further enhancing the stress softening. This pulsatile force into the tissue may increase the compliance of the lesion,

facilitating higher rates of success in angioplasty and stenting, as was observed in the CALCIUM 360 [12], COMPLIANCE 360° [13], and ORBIT I and II [14,15] clinical trials.

2.4.3 Orbital motion in rotational atherectomy

With this presented experimental setup, the grinding wheel motion in rotational atherectomy was investigated which showed a similar orbital motion. Figure 2.9 shows the grinding wheel motion analysis in rotational atherectomy with a 2.5 mm diameter grinding wheel rotating at 160,000 rpm in a 4 mm diameter lumen. Figure 2.9(a) shows the relationship between grinding wheel displacement over time. Nine video images with 2.9 ms time step in the radial and axial directions are shown in Figure 2.9(b). The grinding wheel motion in rotational atherectomy is illustrated schematically in Figure 2.9(c). The wheel rotational and orbital directions are the same. The wheel rotates about its axis and orbits about the vessel axis.

Comparing to the crown motion as shown in Figure 2.5, the rotational atherectomy grinding wheel has the similar low frequency orbital motion, though the high frequency rotation of the connection point between drive shaft and the grinding wheel does not exist because the rotational atherectomy grinding wheel is axisymmetric and coaxially mounted on the drive shaft, as shown in Figure 1.1(a).

2.4.4 Limitations

Currently the absence of any calcified plaque in the region of abrasion stands as a limitation to these results. However, a follow up study wherein calcified plaque will be embedded within a tissue phantom to study the abrasive crown and hardened plaque interaction is planned. Furthermore, the vessel of this study is straight and the flow rate is constant through the current tissue-mimicking phantom. The crown dynamics study in atherectomy needs to be expanded to vessel phantoms with curved geometry, varying diameters, and the pulsatile hemodynamics.

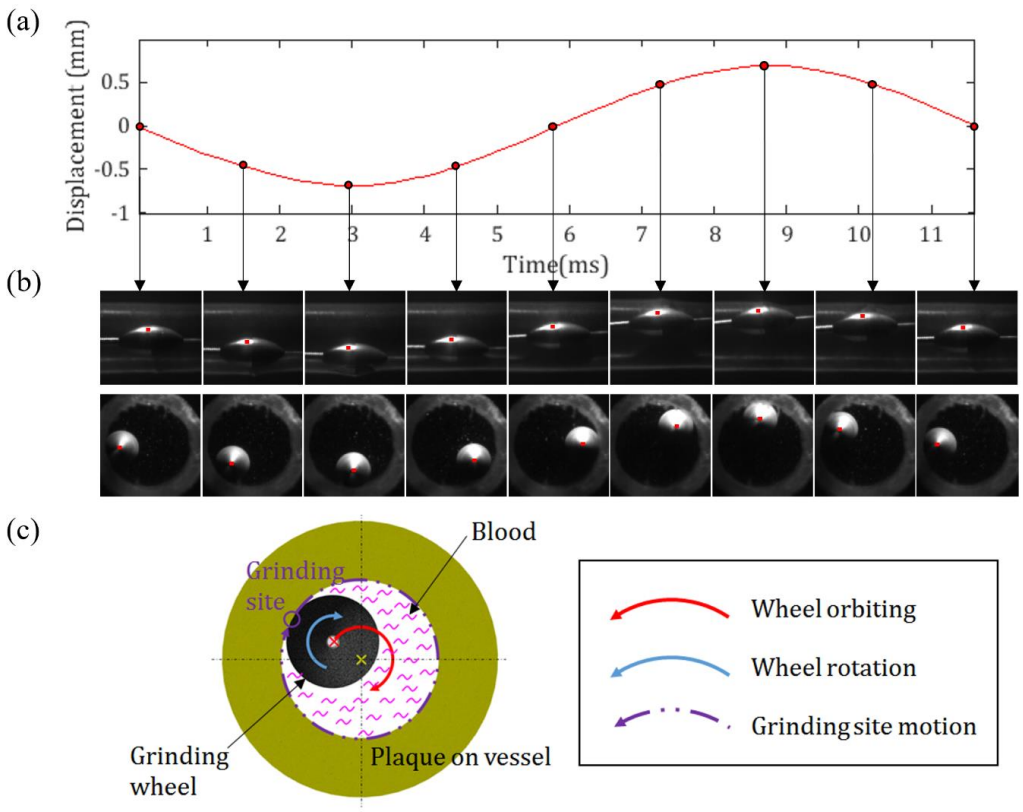

Figure 2.9 Grinding wheel motion analysis in rotational atherectomy: (a) grinding wheel displacement over time and (b) and corresponding video frames in radial- and axial-directions and (c) schematic of the grinding wheel motion in rotational atherectomy.

2.4.5 Conclusions

This work has revealed an important element of crown dynamics in orbital atherectomy, namely that the crown rotates about its axis and orbits around the vessel axis and that this motion results in the rotational and orbital frequencies in the contact forces between the crown and vessel, which could facilitate heat dispersion and tissue softening of the procedure. This study lays the foundation for future research in crown dynamics numerical modeling and the calcified plaque material removal mechanism in orbital atherectomy.

References

[1] Kasapis C, Gurm HS. Current approach to the diagnosis and treatment of femoral-popliteal arterial disease. a systematic review. Curr Cardiol Rev. 2009;5(4):296-311.

[2] Yehuda GW, Zeev K, Laszlo Z. Size of normal and aneurysmal popliteal arteries: a duplex ultrasound study. J Vasc Surg. 2006;43(3):488-92.

[3] McKee CT, Last JA, Russell P, Murphy CJ. Indentation versus tensile measurements of young's modulus for soft biological tissues. Tissue Eng Part B Rev. 2011;17(3):155-64.

[4] Li W, Belmont B, Shih AJ. Design and manufacture of polyvinyl chloride (PVC) tissue mimicking material for needle insertion. In: the 43rd North America Manufacturing Research Conference; Charlotte, NC. 2015; p.866-78.

[5] Kistler Instrumente AG. MiniDyn-multicomponent dynamometer up to 250 N, type 9256C. Product datasheet 2003.

[6] Maher E, Creane A, Sultan S, Hynes N, Lally C, Kelly DJ. Inelasticity of human carotid atherosclerotic plaque. Ann Biomed Eng. 2011;39(9):2445-55.

[7] Lovik RD, Abraham JP, Sparrow EM. Assessment of possible thermal damage of tissue due to atherectomy by means of a mechanical debulking device. In: the 10th ASME Summer Bioengineering Conference (SBC2008); Marco Island, FL. 2008; p.799-800.

[8] Walsh MT, Cunnane EM, Mulvihill JJ, Akyildiz AC, Gijsen FJ, Holzapfel GA. Uniaxial tensile testing approaches for characterisation of atherosclerotic plaques. J Biomech. 2014;47(4):793-804.

[9] Peña E, Peña JA, Doblaré M. On the mullins effect and hysteresis of fibered biological materials: a comparison between continuous and discontinuous damage models. Int J Solids Struct. 2009;46(7):1727-35.

[10] Maher E, Creane A, Lally C, Kelly DJ. An anisotropic inelastic constitutive model to describe stress softening and permanent deformation in arterial tissue. J Mech Behav Biomed Mater. 2012;12:9-19.

[11] Diani J, Fayolle B, Gilormini P. A review on the Mullins effect. Eur Polym J. 2009;45(3):601-12.

[12] Shammas NW, Lam R, Mustapha J, Ellichman J, Aggarwala G, Rivera E, Niazi K, Bala N. Comparison of orbital atherectomy plus balloon angioplasty vs. balloon angioplasty alone in patients with critical limb ischemia: results of the CALCIUM 360 randomized pilot trial. J Endovasc Ther. 2012;19(4):480-8.

[13] Dattilo R, Himmelstein SI, Cuff RF. The COMPLIANCE 360° trial: a randomized, prospective, multicenter, pilot study comparing acute and long-rerm results of orbital atherectomy to aalloon angioplasty for calcified femoropopliteal disease. J Invasive Cardiol. 2014;26(8):355-60.

[14] Bhatt P, Parikh P, Patel A, Chag M, Chandarana A, Parikh R, Parikh K. Orbital atherectomy system in treating calcified coronary lesions: 3-year follow-up in first human use study (ORBIT I trial). Cardiovasc Revasc Med. 2014;15(4):204-8.

[15] Bhatt P, Parikh P, Patel A, Chag M, Chandarana A, Parikh R, Parikh K. Long-term safety and performance of the orbital atherectomy system for treating calcified coronary artery lesions: 5-year follow-up in the ORBIT I trial. Cardiovasc Revasc Med. 2015;16(4):213-6.

CHAPTER 3
COMPUTATIONAL FLUID DYNAMICS MODELING OF THE BURR ORBITAL MOTION IN ROTATIONAL ATHERECTOMY

3.1 Introduction

Rotational atherectomy (RA) experiments in an optically translucent phantom have been conducted in Chapter 2 and the results demonstrated the burr orbits in the same direction as its rotational motion [1]. As shown in Figure 3.1(b), the rotational burr orbits around the artery axis and contacts the arterial wall during RA. The burr rotational speed affects its orbital motion and contact force between the burr and the arterial wall [2]. This observation of burr orbital motion challenges the traditional RA technique to stepwise

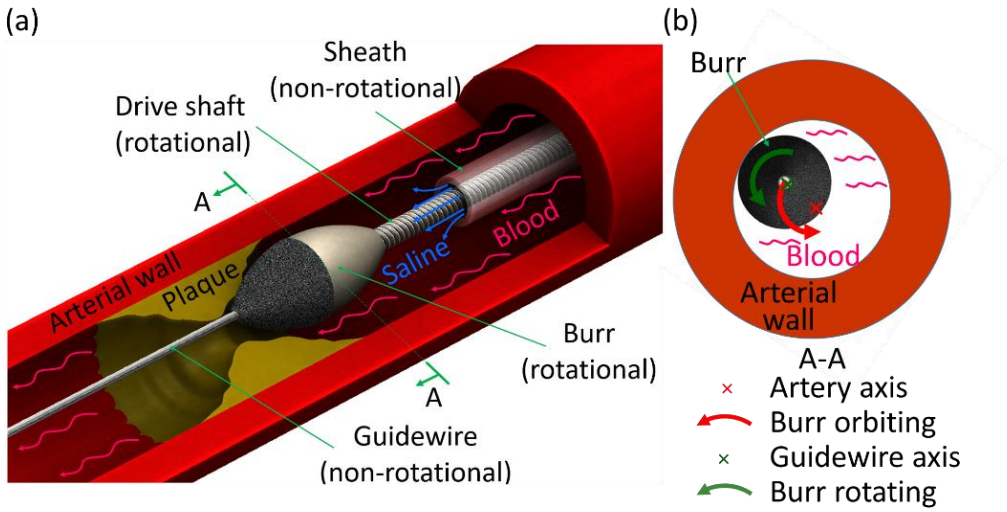

Figure 3.1 (a) Overview of the rotational atherectomy and (b) cross-sectional view of the burr orbital and rotational motion.

increase the burr diameter for removing more plaque and enlarging the lumen size [3-8]. Our literature review in Chapter 1 shows the lack of consensus of the rotational speed and burr to artery ratio (B/A ratio) for RA procedure. It is imperative to gain a better understanding of the burr rotational and orbital motion for various rotational speeds and B/A ratios.

In RA, the burr orbital motion is a result of the blood flow induced by burr rotation [1]. The flow with burr rotation in an artery, omitting the prolate spheroid shape of the burr, can be simplified as the eccentric annular flow with a rotating inner cylinder. Feng *et al.* [9] studied the inner cylinder orbital motion with force equilibrium in 2D. This model is a valuable tool to explain the RA orbital motion. Rotor whirling in turbomachinery, another analogous problem, has been investigated and demonstrated that CFD is an effective tool to predict the fluid forces on the rotor shaft [10-13]. In this study, a 3D CFD model for RA was developed to predict the fluid force of the rotational burr orbiting inside an artery, which is difficult to measure experimentally.

The 3D CFD model was experimentally validated to analyze the burr motion, force, and the associated flow field. The simulation was carried out using re-normalisation group (RNG) theory based k–ε turbulence model for enhanced accuracy for swirling flows [14]. The k–ε model assumes an isotropic eddy viscosity and solves the turbulent kinematic energy (k) and turbulence dissipation rate (ε), which gives a higher accuracy, compared to the Spalart-Allmaras turbulence model where only k is computed [15]. The k–ω model solves k and specific dissipation rate (ω) and is more suitable for low Reynolds number flows [16]. Reynolds stress model [17] is accurate by directly solving the anisotropic turbulence stress but it is computationally expensive and difficult to converge. The burr orbital motion was implemented via introducing a reference frame rotating about the artery axis. The model was validated by the flow field obtained via PIV. With this model, the hydraulic force on the burr was calculated. Effects of the burr rotational speed and the B/A ratio in RA were revealed.

The chapter is organized as follows. Model formulation and numerical solution are first introduced. PIV setup and design of experiment are then presented. The agreement between the CFD model and PIV observation is shown in results, followed by a discussion on the effects of the rotational speed and B/A ratio on the burr dynamics in RA.

3.2 Materials and Methods

3.2.1 CFD formulation

Fluid around the RA burr in the arterial cylinder was modeled as shown in Figures 3.2(a) and (b). The burr has an elliptical shape and the largest diameter is 2.38 mm at the cross section at the equator. The burr's length is 4.8 mm. The arterial cylinder is 10 mm long and 4 or 6 mm in diameter to study RA in the coronary [18] or peripheral [19] artery, respectively. The catheter and artery axes are parallel. Clearance between the burr and the cylindrical arterial wall is 10 μm, which is the average height of the abrasives on the burr surface [1]. Water is the fluid used in the CFD model and PIV experiment considering the blood's Newtonian approximation at a high shear rate [20]. The mass flow rate of the water is 30 g/min. The burr and the drive shaft rotate at rotational speeds ω = 135,000, 145,000, 155,000, 165,000, and 175,000 rpm around the guidewire axis while the guidewire does not rotate. The catheter orbits at the orbital speed Ω = 8,832, 9,210, 9,618, 9,930, and 10,248 rpm in the 4 mm artery and Ω = 4,452, 4,638, 4,836, 5,052, and 5,262 rpm in the 6 mm artery for ω = 135,000, 145,000, 155,000, 165,000, and 175,000 rpm, respectively. These orbital speeds were measured by a high-speed camera [1, 21].

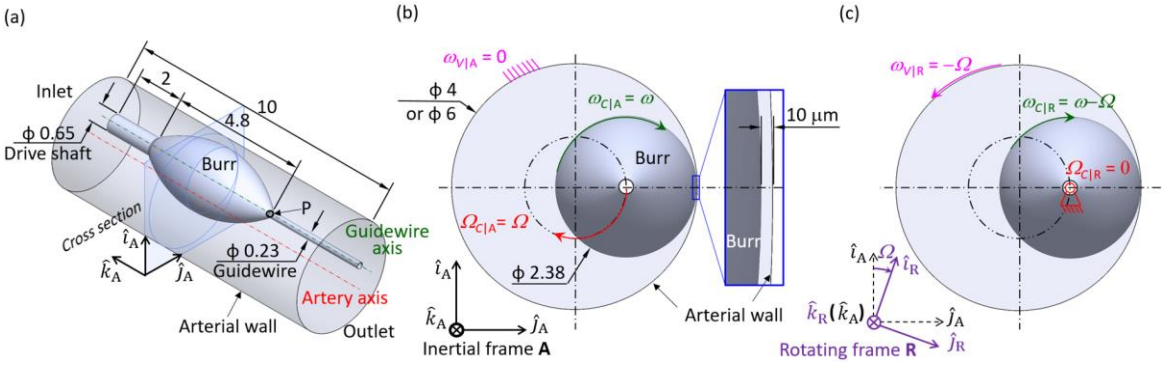

Figure 3.2 RA CFD modeling: (a) catheter in an artery and (b) cross-sectional views of burr rotating and orbiting in an inertial frame and (c) in a rotating frame. (unit: mm)

3.2.2 Governing equations and boundary condition in a rotating reference frame

A rotating reference frame, **R**, was introduced, as shown in Figure 3.2(c), to execute the burr orbital motion without using the dynamic mesh [9]. Relative to the inertial frame **A**, **R** has an angular velocity equal to Ω, as described in Eq. (3.1):

$$[\hat{\imath}_{\mathrm{R}} \quad \hat{\jmath}_{\mathrm{R}} \quad \hat{k}_{\mathrm{R}}] = \begin{bmatrix} \cos(\Omega t) & \sin(\Omega t) & 0 \\ -\sin(\Omega t) & \cos(\Omega t) & 0 \\ 0 & 0 & 1 \end{bmatrix} \begin{bmatrix} \hat{\imath}_{\mathrm{A}} \\ \hat{\jmath}_{\mathrm{A}} \\ \hat{k}_{\mathrm{A}} \end{bmatrix} \tag{3.1}$$

where $\hat{\imath}$, $\hat{\jmath}$,and $\hat{k}$ are mutually orthogonal unit vectors defining the Cartesian frames. Governing equation of motion of the incompressible flow in a rotating reference frame is:

$$\frac{\partial \vec{u}}{\partial t} + \vec{u} \cdot \nabla \vec{u} = -\frac{1}{\rho} \nabla P + \nu \nabla^2 \vec{u} + \vec{f} - \vec{\Omega} \times \left(\vec{\Omega} \times \vec{r}\right) - 2\vec{\Omega} \times \vec{u} \tag{3.2}$$

where $\vec{r}$ and $\vec{u}$ are the fluid particle location and velocity vectors observed in **R**, respectively; $\vec{f}$ is the external force acting on the fluid; $\vec{\Omega}$ is the angular velocity of **R** relative to **A**; and t, ρ, P, and ν represent time, density, pressure, and kinematic viscosity, respectively. In this study, $\vec{f} = 0$ and $\vec{\Omega} = [0 \quad 0 \quad \Omega]^{\mathrm{T}}$. The last two terms on the right side of Eq. (3.2) are introduced due to the centrifugal and Coriolis effects in a rotating coordinate system.

The continuity equation is:

$$\nabla \cdot \vec{u} = 0 \tag{3.3}$$

As demonstrated in Figures 3.2(b) and (c), the boundary conditions altered with the change of frame from **A** to **R**. The arterial wall in **A** is stationary, so the angular velocity of the arterial wall in frame A, $\omega_{V|\mathrm{A}}$, = 0. In **R**, the arterial wall has an angular velocity $\omega_{V|\mathrm{R}} = -\Omega$. The catheter rotational speed in **A**, $\omega_{C|\mathrm{A}}$, = ω, while in **R**, $\omega_{C|\mathrm{R}} = \omega - \Omega$. The burr orbits in A at $\Omega_{C|\mathrm{A}} = \Omega$ and has no orbital motion in **R**, $\Omega_{C|\mathrm{R}} = 0$.

3.2.3 Numerical method

The CFD software, Fluent (v16.2, ANSYS Inc., Canonsburg, PA, US), was used to solve the 3D steady incompressible Navier-Stokes equations. In this rotation-dominant flow, to determine the turbulent effects, Taylor number, Ta, was calculated [22]:

$$Ta = \omega^2 r(R-r)^3 \nu^{-2} \quad (3.4)$$

where ω is the characteristic angular velocity and in this case the burr rotational speed and r and R are the radius of the burr's radius at its equator and the arterial wall, respectively. With r = 1.19 mm, R = 2 mm, and ω = 135,000 rpm, $Ta = 1.25\times10^8$, which is well above the critical value of 1,700 for the turbulent flow [23]. The RNG k–ε turbulence model was adopted to solve the swirling flows [14]. Enhanced wall function was utilized to increase the computing accuracy within the boundary layer. The second order scheme was applied to discretize the pressure, momentum, turbulent kinetic energy, and turbulent dissipation rate. Semi-implicit pressure linked equations were utilized to handle the velocity-pressure coupling. The convergence criterion was 10^{-4} for the residuals of continuity, momentum, and the turbulent transport equations.

The mesh was generated using the software Pointwise (v17.3, Pointwise Inc., Fort Worth, TX, US) with 1.23 million tetrahedron cells. Near the walls, 0.2 million prism cells were introduced to mesh the viscous sublayer. For grid independence test, two additional uniformly refined meshes with 2.23 and 5.21 million cells were created, showing an L^2 relative error norm of the velocity less than 3%.

3.2.4 Experimental setup

The PIV experiment was carried out to measure the fluid flow near the burr. The highest and lowest rotational speeds, 175,000 and 135,000 rpm, were tested during RA in two phantoms with 4 and 6 mm artery diameter. In total, four PIV cases were conducted. These cases are numbered as Case 1 (135,000 rpm in 4 mm), Case 2 (175,000 rpm in 4 mm), Case 3 (135,000 rpm in 6 mm), and Case 4 (175,000 rpm in 6 mm). Results obtained from those four PIV cases were used to validate the CFD model.

The experimental setup, as shown in Figure 3.3, consisted of three modules: RA device, arterial phantom, and PIV system.

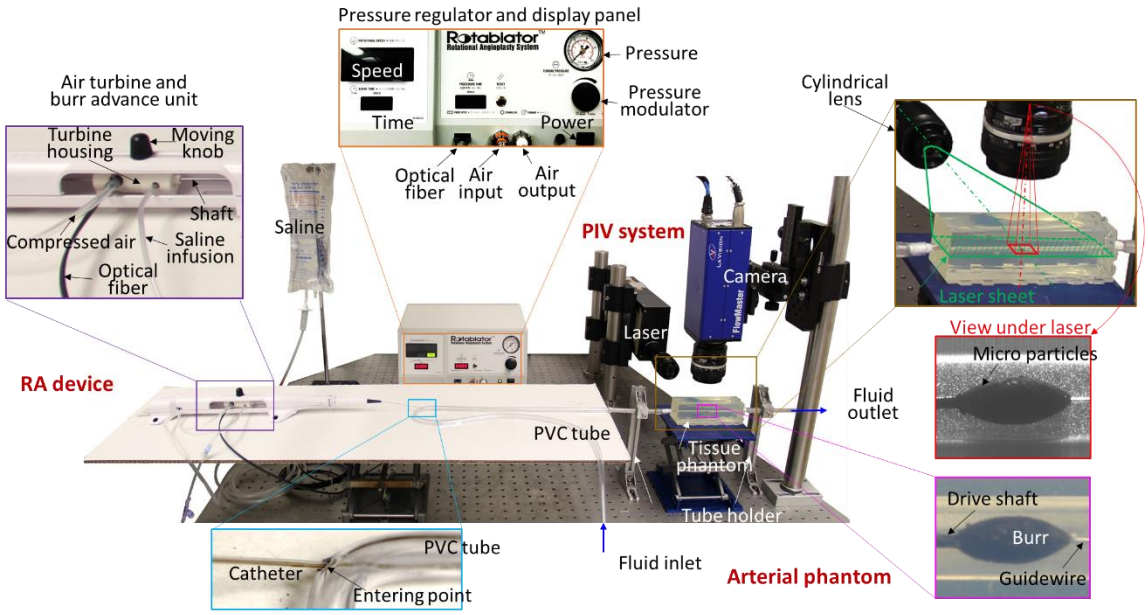

Figure 3.3 PIV experimental setup.

3.2.4.1 RA device

The RA device (Rotablator™ by Boston Scientific, Marlborough, MA, US) consists of a catheter, an air turbine, a burr advance unit, and a pressure regulator. The catheter (Figure 3.1(a)) is inserted into the patient's artery during RA. In this study, the catheter was equipped with a 2.38 mm diameter burr. Detailed dimensions of the RA catheter can be found in [1,2]. The drive shaft is driven by an air turbine. As shown in Figure 3.3, the compressed air from the pressure regulator drives the air turbine. The air pressure is adjusted to control the turbine rotational speed via the pressure modulator. Saline is infused into the sheath from the side of the air turbine and burr advance unit.

3.2.4.2 Arterial phantom

The RA catheter was inserted in a PVC tube through a side hole, as shown in Figure 3.3. The PVC tube with water running through was used to simulate the artery with blood flow. The fluid was pumped through the arterial phantom at 30 g/min (as in the CFD model) via a roller pump combined with a 2 m long soft Latex rubber tube to absolve the pulsatile wave. The tube was connected to a cuboid tissue phantom made of transparent PVC [21] for PIV imaging. Phantoms with a hole of 4 or 6 mm diameter were used to simulate the

coronary or peripheral artery, respectively. The burr was placed at the center inside the phantom artery, as shown in Figure 3.3.

3.2.4.3 PIV measurement system

As shown in Figure 3.3, the dual pulse Nd:YAG laser beam (523 nm wavelength, Solo III 15 Hz, New Wave Inc., Fremont, CA, US) passing through a cylindrical lens (Modular-Focus, f = 6 mm, Rodenstock GmbH Co., München, Germany) illuminated a horizontal plane aligned with the artery axis. The phantom artery was filled with a 30% sucrose water solution to minimize refraction [24]. The fluid was seeded with 10 μm diameter neutrally buoyant hollow Borosilicate glass spherical micro particles (Dantec Dynamics A/S, Skovlunde, Denmark). The micro particles were illuminated by laser. Reflections from the RA burr and drive shaft were minimized by painting both components black. The guidewire was not painted so that it could reflect and be used to locate the burr during image processing. A CCD camera (Flowmaster 3S, LaVision Inc., Goettingen, Germany) was mounted above the arterial phantom with the focal plane aligned to the laser sheet. A sample image under laser illumination is shown in Figure 3.3. The camera collected image pairs at a rate of 4 Hz with a time-delay of 10 or 20 μs for the 4 and 6 mm arterial phantoms, respectively. Timing of the laser and camera were controlled by a PC-based timing unit and software (DaVis, LaVision Inc., Goettingen, Germany). Images were recorded during each experiment for 100 s, resulting in 400 image pairs per experiment.

3.2.5 Image processing

The burr position varied from one image pair to another, because the burr orbital frequency differed from the imaging frame rate (4 Hz), as shown in Figure 3.4(a). Shadow of the burr causing poor particle illumination may impair the PIV analysis. A burr position tracking algorithm written in MATLAB (R2016a, The MathWorks Inc., Natick, MA, US) was used to group image pairs with identical burr positions (away from the laser to avoid burr shadow).

Steps for PIV analysis for Case 1 is illustrated in Figure 3.4. The point P in Figure 3.4(a) is where the burr connects to the guidewire. The location of P was identified by the

difference in intensity of burr and guidewire in images (Figure 3.4(b)). The guidewire region was identified as a group of high intensity pixels with the size of the group greater than 0.1×0.1 mm. The P position, defined as the left-most pixel in this group, was tracked for every image in the sequence as shown in Figure 3.4(c) resulting in a set of 400 P and burr locations (Figure 3.4(d)). A 25 μm slit (marked within two red dash lines in Figure 3.4(d)) near the far wall was selected to identify images with the burr located away from the laser source to minimize the burr shadow. For Case 1, a total of 9 images (and P marked within the two red dash lines in Figure 3.4(d)) were chosen. Three of the 9 images are

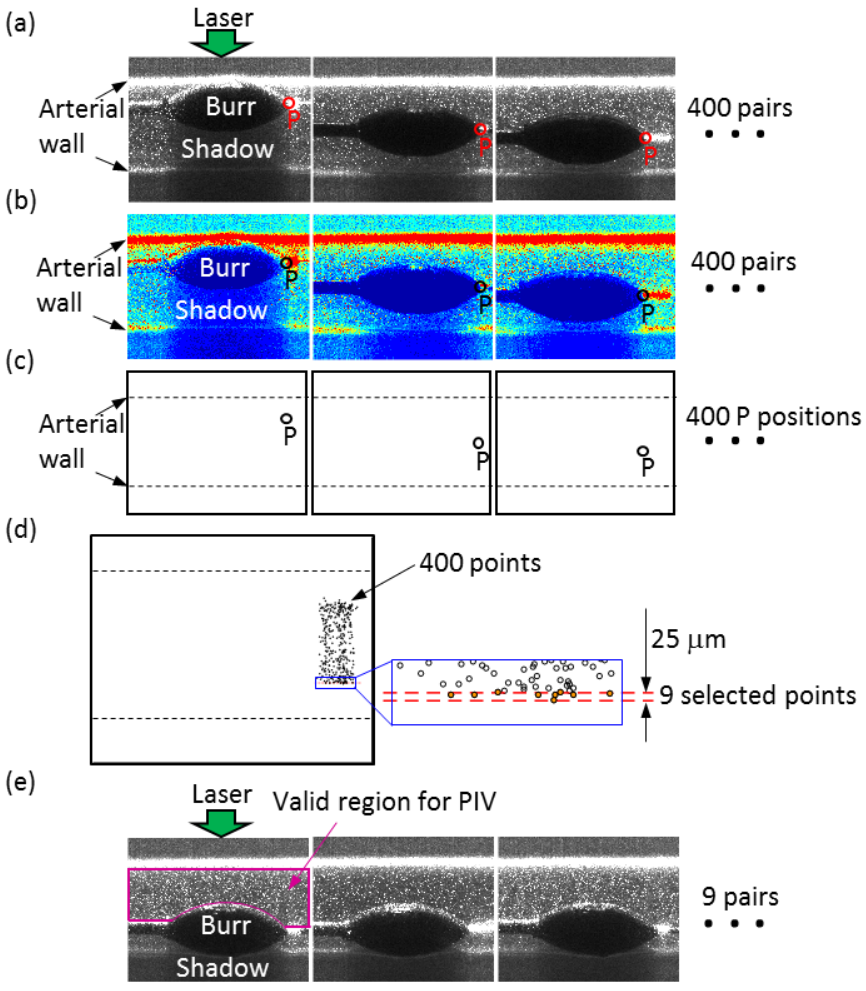

Figure 3.4 PIV analysis for Case 1: (a) original images, (b) images with 10 levels of pixel intensity to highlight P, (c) P positions, (d) selection of images with P location in the 25 μm slit, and (e) selected images for PIV analysis.

shown in Figure 3.4(e). For Cases 2, 3, and 4, a total of 8, 8, and 7 image pairs, respectively, were identified in the 25 μm slit for PIV analysis. A slit width sensitivity test was conducted on Case 1. With a slit width of 13, 25, and 37 μm, 6, 9, and 11 image pairs were selected, effects of which are shown in Figure 3.7.

The selected image pairs were analyzed by a MATLAB-based package, PIVlab 1.41 [25]. A region of interest was selected to exclude the arterial wall. This region was divided into 64×64 pixel interrogation windows with 50% overlap. This window size includes about 13 micro particles for analysis accuracy and resolution [26]. Displacement estimation for each interrogation window was performed using an FFT-based cross-correlation algorithm with window deformation [25]. Velocity vectors were calculated from this displacement estimate and the time delay of the image pair. Vectors with components 7 standard deviations away from the global mean were removed as global outliers and were replaced by Laplace interpolation. Noise was further eliminated using a 3×3 local median filter.

3.3 Results

Figures 3.5 and 3.6 show the CFD and PIV flow field with 4 and 6 mm lumen, respectively. For each case, the velocity vectors and the magnitude based color map are presented with PIV above the CFD results, and the radial and axial components of the velocity vectors along a probing line are shown at the bottom of the figure, with the mean and one standard deviation of PIV marked in red and CFD result in black. The probing line is located in the middle of the gap between the burr and the arterial wall with the axial position "0" at the burr's equator.

As shown in the velocity vector field, high speed regions (with red background) mainly exist around the burr, confirming this rotation dominated flow. Four vortices can be observed in all the cases: a pair of counter-rotating vortices near the burr equator and two of relatively large size at the upstream and downstream edge of the field. The counter-rotating pair develops in the same manner as the Taylor-Couette flow [27]. With the same artery diameter, higher burr rotational speed increases the size of the vortices near the burr

and spreads the high speed region further away from the burr surface. With the same burr rotational speed, in a smaller artery, the vortices near the burr shrink due to the arterial wall constraint and the high speed region extends more in the axial direction. These observations are consistent between CFD results and PIV. Noise exists around the burr and the drive shaft in PIV because the out-of-imaging-plane components with large magnitudes were captured due to the thickness of the laser sheet.

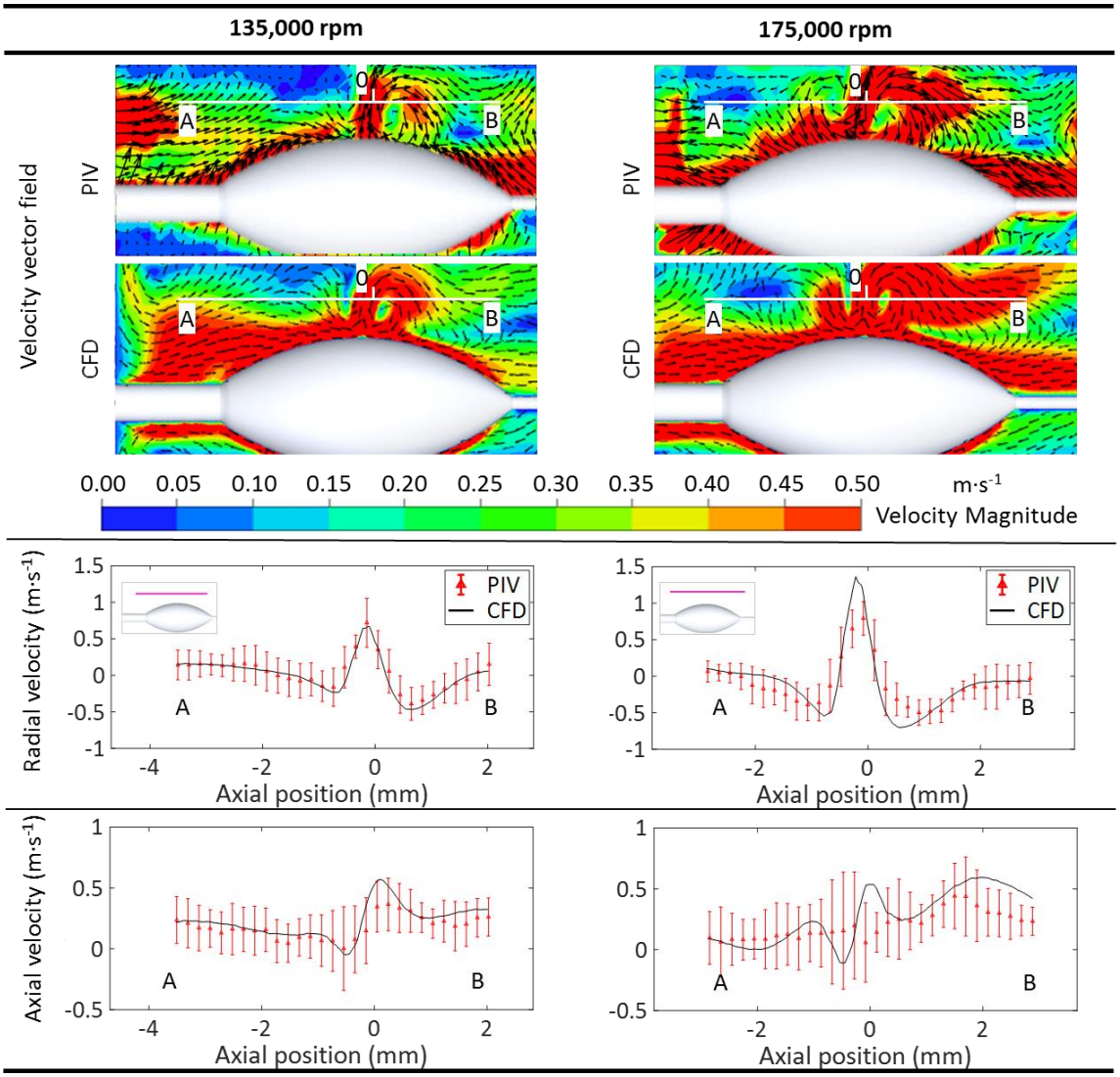

Figure 3.5 Flow field from CFD and PIV analysis (4 mm artery diameter).

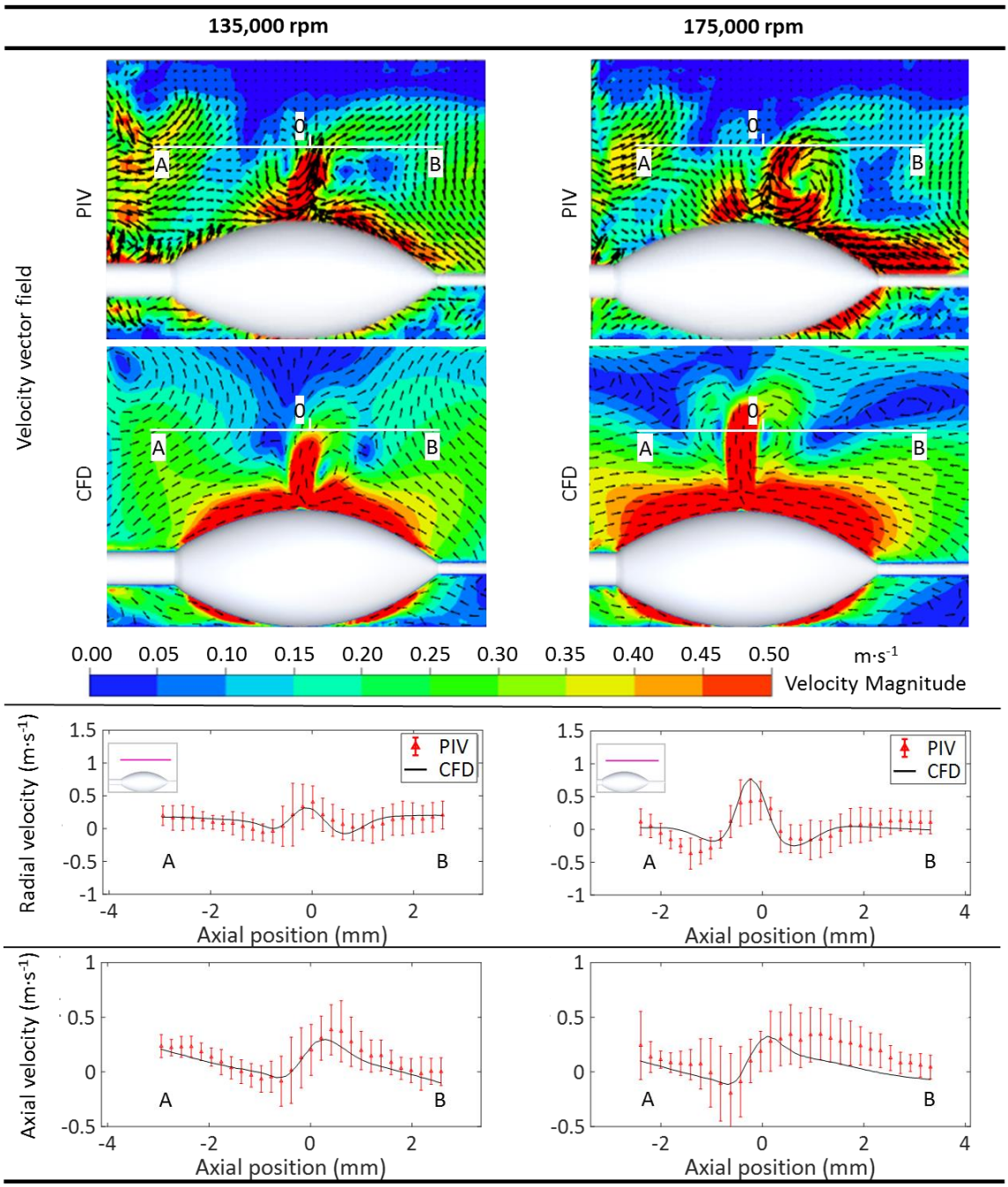

Figure 3.6 Flow field from CFD and PIV analysis (6 mm artery diameter).

The radial and axial velocities along the probing line quantitatively manifest the agreement between CFD results and PIV. The CFD value lies within one standard deviation from the mean PIV measurement at most positions. Large velocity gradient is difficult to be captured by PIV due to the limited spatial resolution which explains the peak and valley mismatch in the 175,000 rpm cases.

Sensitivity test result on the slit width for image pair selection is shown in Figure 3.7. Along the probing line AB in Case 1 (Figure 3.5), the axial speed calculated from image pairs selected by 13 and 37 μm slit relative to 25 μm slit has 6% and 2% root mean square difference in mean values, and 4% and 2% root mean square difference in standard deviations, respectively. The slit width for image pair selection does not affect the agreement between CFD and PIV analysis.

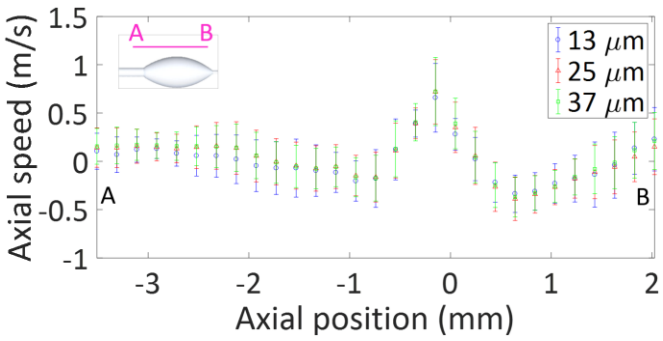

Figure 3.7 Effect of the slit width for image pair selection on Case 1.

With this validated model, the pressure field was examined to better understand the flow and the motion of the burr. As shown in Figure 3.8(a), pressure near the burr is lower due to the large rotational speed of the burr. Pressure distribution at two cross sections C-C and D-D, as shown in Figure 3.8(b), also shows that pattern. Streamlines are circles around the artery axis due to the strong rotational motion. The flow forms a high pressure region before entering the gap and a low pressure region after exiting the gap. This pressure difference drives the burr orbital motion. The high pressure region is larger in C-C where the gap is narrower (10 μm compared to 33 μm in D-D). As shown in Figure 3.8(c), at the gap, C-C has a larger local maximum pressure, a smaller local minimum pressure, and a larger pressure gradient compared to D-D. The local minimum pressure is where the gap converges to its narrowest area. As shown in Figure 3.8(d) the pressure difference is larger when the gap is narrower. Therefore, the hydraulic force on the burr concentrates in the narrowest gap area.

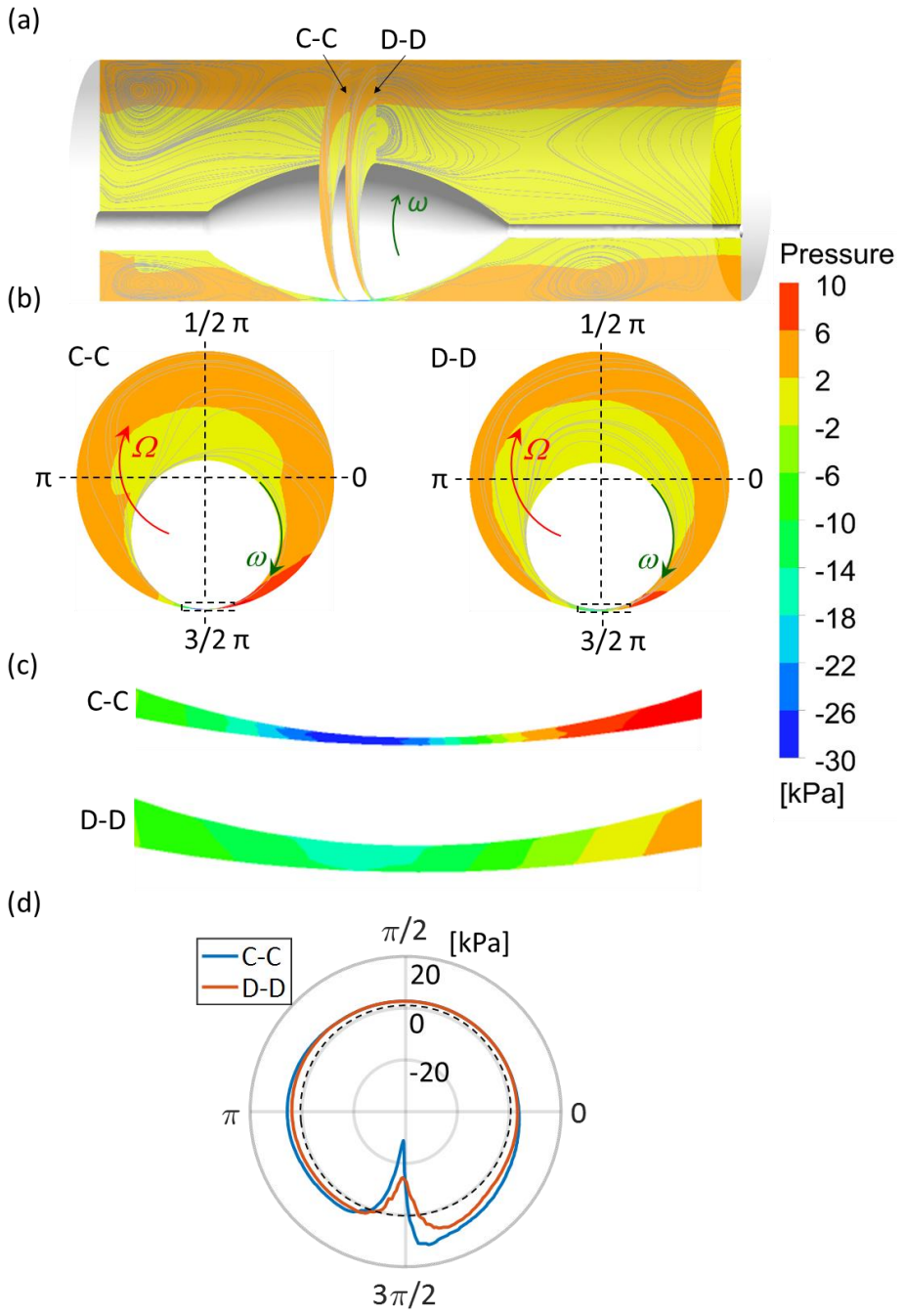

Figure 3.8 Pressure distributions in Case 1 (4 mm artery diameter and 135,000 rpm): (a) axial view and two cross-sectional view of pressure and streamlines, (b) cross sectional view of pressure and streamlines in C-C (with the minimum 10 μm gap) and D-D (0.45 mm away from C-C with 33 μm gap), (c) pressure distribution in the gaps in C-C and D-D, and (d) polar plot of pressure distributions in cross sections C-C and D-D.

Shear rate of the fluid near the burr is high, over 1000 s^{-1}. Merrill *et al.* [20] has proved that human blood behaves as a Newtonian fluid if the shear rate exceeds about 100 s^{-1}. For the example of Case 3, as shown in Figure 3.9, almost all fluid region has the shear rate higher than 100 s^{-1} and justifies the Newtonian fluid assumption in CFD analysis.

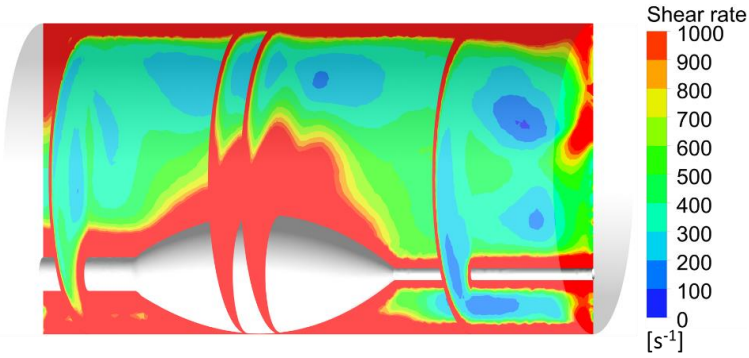

Figure 3.9 Shear rate in Case 3 (6 mm lumen and 135,000 rpm).

3.4 Discussions

3.4.1 Forces

The fluid generates a hydraulic force ($\boldsymbol{F_H}$) on the rotating and orbiting burr with directions illustrated in Figure 3.10(a). $\boldsymbol{F_H}$ on the burr can be calculated by integrating the CFD pressure and shear stress on burr surface. In addition to $\boldsymbol{F_H}$, a contact force $\boldsymbol{F_C}$ exists between the burr and arterial wall. The orbiting burr is also subject to the centrifugal force $\boldsymbol{F_\Omega}$. Forces on the burr ($\boldsymbol{F_H}$, $\boldsymbol{F_C}$, and $\boldsymbol{F_\Omega}$) are summarized in Figure 3.10(b). $\boldsymbol{F_H}$ and $\boldsymbol{F_C}$ are decomposed to the tangential and normal directions ($F_{H,t}$ and $F_{H,n}$) and ($F_{C,t}$ and $F_{C,n}$), as shown in Figure 3.10(b). The balance of force components on the burr in tangential and normal directions can be expressed as:

$$F_{C,t} - F_{H,t} = 0 \tag{3.5}$$

and

$$F_{C,n} - F_{H,n} - F_{\Omega} = 0 \tag{3.6}$$

where $F_\Omega (= m(R-r)\Omega^2)$ is the centrifugal force, m is the mass of the burr. In this study, m = 0.11 g.

The arterial wall is subject to the force $\boldsymbol{F_C}$, as shown in Figure 3.10(c). $\boldsymbol{F_C}$ is critical in RA since large $\boldsymbol{F_C}$ may lead to dissection, vasospasm, or large debris size (resulting the blockage of microvessel and slow-flow or no-reflow conditions) [28,29]. $\boldsymbol{F_C}$ is difficult to be measured experimentally, but can be estimated by using Eqs. (3.5) and (3.6).

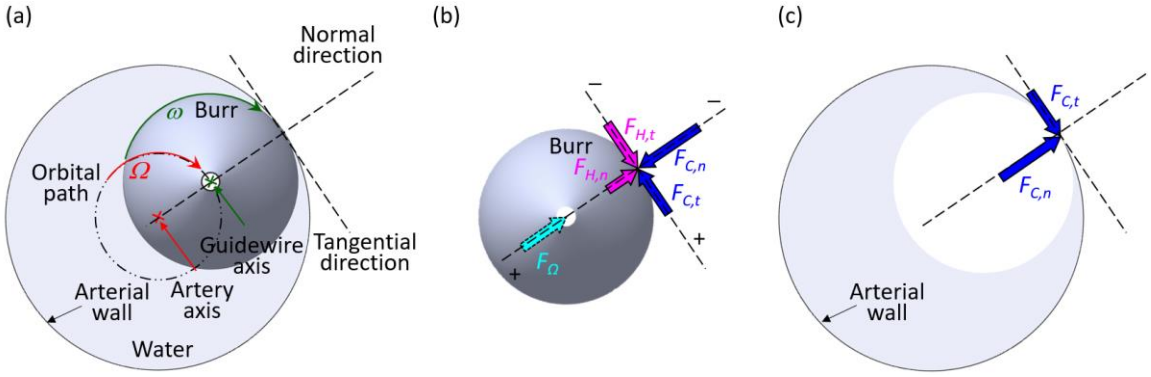

Figure 3.10 Forces in RA: (a) burr orbital and rotational directions and the tangent and normal directions, (b) force on the burr, and (c) force on the arterial wall.

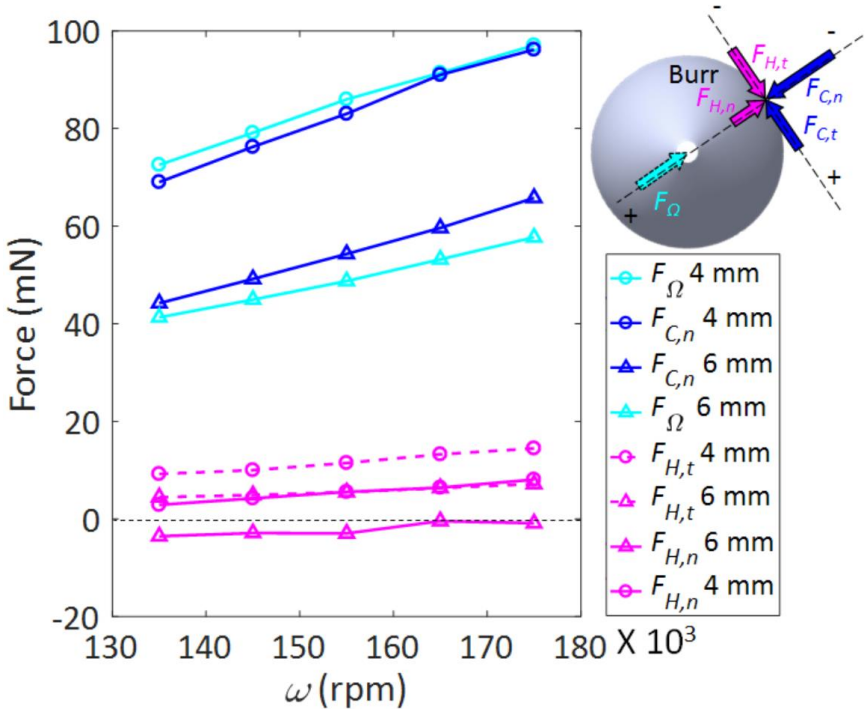

Figure 3.11 Centrifugal force, contact force, and hydraulic force on the burr.

Figure 3.11 shows values of the F_{Ω}, $F_{H,t}$, $F_{H,n}$, $F_{C,t}$ and $F_{C,n}$ on the burr under 5 rotational speeds in 4 and 6 mm artery diameters (with 0.4 and 0.6 B/A ratio, respectively).

In the normal direction, F_{Ω} increases with the rotational speed due to the higher orbital speed. F_{Ω} is larger in the 4 mm (relative to the 6 mm) artery diameter also due to the higher orbital speed. The hydraulic force $F_{H,n}$ is much smaller (less than 15%) than F_{Ω}. In the 4 mm artery, $F_{H,n}$ is negative (pointing toward the artery axis) and decreases with the rotational speed. In the 6 mm artery, $F_{H,n}$ is positive (pointing toward the arterial wall) and increases with the rotational speed. The contact force $F_{C,n}$ is dominated by F_{Ω} and has a similar trend as F_{Ω}. $F_{C,n}$ in the 4 mm artery with a rotational speed of 135,000 rpm is larger than that in the 6 mm artery with a rotational speed of 175,000 rpm. This indicates that the artery diameter is the dominant factor on the contact force comparing to the rotational speed. $F_{C,n}$ has a maximum value of 96.2 mN for Case 2 (4 mm artery and 175,000 rpm) and minimum value of 44.2 mN for Case 3 (6 mm artery and 135,000 rpm).

In the tangential direction, $F_{H,t}$ consistently points toward the orbital direction (+ in the tangent direction) in all cases. $F_{C,t}$ has the same magnitude but an opposite direction of $F_{H,t}$. $F_{H,t}$ increases with the rotational speed and increases at a higher rate in the 4 mm artery. $F_{H,t}$ in the 4 mm artery is larger than that in the 6 mm artery. $F_{H,t}$ in the 4 mm artery with a rotational speed of 135,000 rpm is even higher than that in the 6 mm artery with a rotational speed of 175,000 rpm. This once again indicates the artery diameter is a dominating factor in the tangential hydraulic and contact forces. $F_{H,t}$ had a maximum value of 14.5 mN for Case 2 (4 mm artery and 175,000 rpm) and a minimum value of 4.5 mN for Case 3 (6 mm artery and 135,000 rpm).

3.4.2 Film thickness

The minimum film thickness, H_{min}, of the fluid between a high-speed rotating disk inside a stationary cylinder has been studied experimentally using water as the fluid and can be expressed as the following empirical equation [30]:

$$H_{min} = 7.43 R_E U^{0.65} W^{-0.21} (1 - 0.85 e^{-0.31k}) \tag{3.7}$$

where R_E is the effective radius; U is the dimensionless speed parameter, measuring the flow speed within the contact region; W is the dimensionless load parameter proportional to $F_{C,n}$; and k is the ellipticity parameter, estimated by a curve fit equation [31]. Both of R_E and k are determined by the geometry of the burr and the arterial wall. The value of H_{min} in 4 mm and 6 mm arteries, as shown in Table 3.1, are all around 10 μm. This matches with the 10 μm gap distance assumption. H_{min} is comparable with the measured surface roughness of the burr (10 μm) [1], which indicates that the burr is partially in contact with the arterial wall via the abrasive grits – also known as the partial lubrication [32].

Table 3.1 Values of H_{min} for both of the arteries under 5 rotational speeds.

Variable (unit)	Artery diameter	Rotational speed (rpm)				
		135,000	145,000	155,000	165,000	175,000
H_{min} (μm)	4 mm	9.6	9.8	10.0	10.2	10.5
	6 mm	11.0	11.2	11.4	11.7	11.9

3.5 Conclusions

A CFD model of the rotating burr orbital motion in RA was established and validated by PIV results. The centrifugal force dominated the contact force between the burr and the artery wall. Both hydraulic and contact forces increase with the burr rotational speed (from 135,000 to 175,000 rpm) and the B/A ratio (0.4 and 0.6). To reduce the contact force during RA, clinicians may use a smaller burr with a lower rotational speed, which, however, may result in larger debris and needs trade-off and further investigation. This CFD model facilitates to understand the burr dynamics and RA techniques from the fluid mechanics perspective.

There are three limitations for the current study. First, the rotating axis of the burr was assumed to be parallel to the arterial axis due to the constraint of the guidewire, though the burr's axial translation and yaw/pitch rotations were observed. In RA, the burr axial translation speed (0.01 m/s) was minimal compared to the burr surface speed (over 16.8 m/s) and may not have a significant effect. Second, in the practical atherosclerotic lesion

environment, the lumen geometry is irregular and the blood flow is pulsatile. The CFD model was simplified with a circular lumen and steady flow. Third, a small deformation of the arterial wall near the contact area was observed but not considered in the CFD model.

References

[1] Shih A, Liu Y, Zheng Y. Grinding wheel motion, force, temperature, and material removal in rotational atherectomy of calcified plaque. CIRP Ann - Manuf Techn. 2016;65(1):345-8.

[2] Zheng Y, Liu Y, Liu Y, Shih AJ. Experimental investigation of the grinding force in rotational atherectomy. In: Proc. of the 44th SME North American Manufacturing Research Conference; 2016; Blacksburg, VA.

[3] Mota P, de Belder A, Leitão-Marques A. Rotational atherectomy: Technical update. Rev Port Cardiol. 2015;34(4):271-8.

[4] vom Dahl J, Dietz U, Haager PK, Silber S, Niccoli L, Buettner HJ, *et al*. Rotational atherectomy does not reduce recurrent in-stent restenosis: results of the angioplasty versus rotational atherectomy for treatment of diffuse in-stent restenosis trial (ARTIST). Circulation. 2002;105(5):583-8.

[5] Sakakura K, Taniguchi Y, Matsumoto M, Wada H, Momomura S, Fujita H. How should we perform rotational atherectomy to an angulated calcified lesion?. Int Heart J. 2016;57(3):376-9.

[6] Zhang B, Wang F, Tan JW, Liao H, Chai W, Yu H, *et al*. The application of rotational atherectomy in PCI of coronary chronic total occlusions. ASEAN Heart J. 2016;24(1):1-4.

[7] Kuramitsu S, Hiromasa T, Jinnouchi H, Domei T, Shirai S, Ando K. Usefulness of rotational atherectomy with optical frequency domain imaging guidance for severe calcified coronary lesions after Kawasaki disease. Cardiovasc Interv Ther. 2016. [Epub ahead of print].

[8] Lasala JM, Reisman M. Rotablator plus stent therapy (rotastent). Curr Opin Cardiol. 1998;13(4):240-7.

[9] Feng S, Li Q, Fu S. On the orbital motion of a rotating inner cylinder in annular flow. Int J Numer Meth. Fluids. 2007;54(2):155-73.

[10] Moore JJ, Palazzolo AB. Rotordynamic force prediction of whirling centrifugal impeller shroud passages using computational fluid dynamic techniques. J Eng Gas Turbines Power. 1999;123(4):910-8.

[11] Moore JJ, Ransom DL, Viana F. Rotordynamic force prediction of centrifugal compressor impellers using computational fluid dynamic techniques. J Eng Gas Turbines Power. 2010;133(4):042504.

[12] Ha TW, Choe BS. Numerical simulation of rotordynamic coefficients for eccentric annular-type-plain-pump seal using CFD analysis. J Mech Sci Technol. 2012;26(4):1043-8.

[13] Untaroiu A, Untaroiu CD, Wood HG, Allaire PE. Numerical modeling of fluid-induced rotordynamic forces in seals with large aspect ratios. J Eng Gas Turbines Power. 2012;135(1):012501.

[14] Escue A, Cui J. Comparison of turbulence models in simulating swirling pipe flows. Appl Math Model. 2010;34(10):2840-9.

[15] Spalart PR, Allmaras SR. A one-equation turbulence model for aerodynamic flows. Rech Aerospatiale. 1994;1:5-21.

[16] Wilcox DC. Formulation of the k-omega turbulence model revisited. AIAA J. 2008;46(11):2823-38.

[17] Launder BE, Reece GJ, Rodi W. Progress in the development of a Reynolds-stress turbulence closure. J Fluid Mech. 1975;68(3):537-66.

[18] Dodge JT Jr, Brown BG, Bolson EL, Dodge HT. Lumen diameter of normal human coronary arteries. Influence of age, sex, anatomic variation, and left ventricular hypertrophy or dilation. Circulation. 1992;86(1):232-46.

[19] Wolf YG, Kobzantsev Z, Zelmanovich L. Size of normal and aneurysmal popliteal arteries: a duplex ultrasound study. J Vasc Surg. 2006;43(3):488-92.

[20] Merrill EW, Pelletier GA. Viscosity of human blood: transition from Newtonian to non-Newtonian. J Appl Physiol. 1967;23(2):178-82.

[21] Zheng Y, Belmont B, Shih AJ. Experimental investigation of the abrasive crown dynamics in orbital atherectomy, Med Eng Phys. 2016;38(7):639-47.

[22] White MF. Fluid Mechanics. 4th ed. Boston: McGraw-Hill; 1994. 736 p.

[23] Taylor GI. Stability of a viscous liquid contained between two rotating cylinders. Philo Trans R Soc A. 1923;223:289-343.

[24] Charles DF. Refractive indices of sucrose-water solutions in the range from 24 to 53% sucrose. Anal Chem. 1965;37(3):405-6.

[25] Thielicke W, Stamhuis EJ. PIVlab–towards user-friendly, affordable and accurate digital particle image velocimetry in MATLAB. J Open Res Softw. 2014;2(1):e30.

[26] Keane RD, Adrian RJ. Theory of cross-correlation analysis of PIV images. Appl Sci Res. 1992(49)3:191-215.

[27]Larson RG, Shaqfeh ES, Muller SJ. A purely elastic instability in Taylor–Couette flow. J Fluid Mech. 1990;218:573-600.

[28] Tomey MI, Kini AS, Sharma SK. Current status of rotational atherectomy. J Am Coll Cardiol Intv. 2014;7(4):345-53.

[29] Barbato E, Carrié D, Dardas P, Fajadet J, Gaul G, Haude M, *et al*. European expert consensus on rotational atherectomy. EuroIntervention. 2015;11(1):30-6.

[30] Hamrock BJ, Dowson D. Elastohydrodynamic lubrication of elliptical contacts for materials of low elastic modulus I—Fully flooded conjunction. J Lubr Technol. 1978;100(2):236-45.

[31] Hamrock BJ, Brewe D. Simplified solution for stresses and deformations. J Lubr Technol. 1983;105(2):171-7.

[32] Hamrock BJ, Schmid SR, Jacobson BO. Fundamentals of Fluid Film Lubrication. Boca Raton: CRC Press; 2004. 728 p.

CHAPTER 4
MODELING OF THE GRINDING FORCE IN ROTATIONAL ATHERECTOMY USING THE MULTI-GRAIN SMOOTHED PARTICLE HYDRODYNAMICS SIMULATION

4.1 Introduction

As has been demonstrated in Chapters 2 and 3, during rotational atherectomy (RA), the grinding wheel orbits about the artery and contacts the vessel wall while advancing axially through the lesion, resulting in a helix path, as shown in Figure 4.1. Building on this finding, in this chapter, we examined and analyzed the grinding wheel abrasive surface topography, kinematics of the abrasive-workpiece interaction, and grinding force by experiments and smoothed particle hydrodynamics (SPH) simulation.

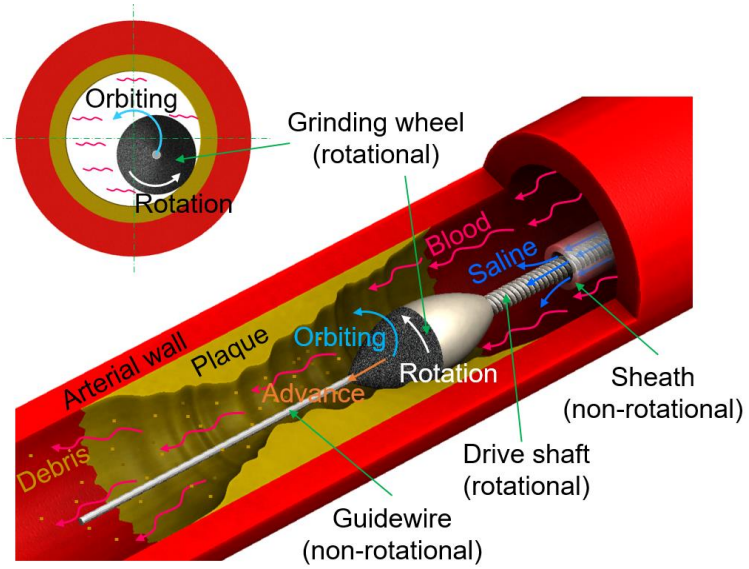

Figure 4.1 Grinding of plaque in rotational atherectomy.

SPH, a meshfree numerical method, has been applied in grinding simulation because of its advantage in modeling large local distortions. Rüttimann *et al*. [1] utilized the SPH model to predict the influence of abrasive geometry on grinding force and debris formation. Shen *et al*. [2] utilized SPH modeling to study the grinding force with various wheel speeds and abrasive rake angles. Cao *et al*. [3] investigated the material removal mechanism in ultrasonic-assisted grinding of hard and brittle materials using SPH. Su *et al*. [4] expanded the SPH method to study the chip formation and workpiece deformation for different abrasive geometry and material and cutting depth and speed. Liu *et al*. [5] investigated the workpiece surface micro-crack generation and propagation in silicon carbide grinding based on the SPH simulation. Our review indicates that SPH is an effective method to predict the grinding of brittle materials. However, these studies using SPH for grinding process modeling [1-5] were all based on the single grain scratch, which omitted grinding wheel topography, rubbing and plowing effects, and workpiece surface geometry during grinding.

Multi-grain grinding simulation has been carried out in the following four studies. Zhang *et al*. [6] presented the finite element modeling of four abrasive grains on a wheel for the grinding of cemented carbide. Based on molecular dynamics modeling, Eder *et al*. [7] investigated the surface finishing after nano-scale grinding with 16 abrasive grains. Rüttimann *et al*. [8] applied the SPH method to simulate two abrasive grains grinding and the burr generation and work-material hardening. Shen *et al*. [9] simulated three abrasive grains grinding using SPH and found the interactions and interferences among grains influenced the grinding force and chip pile-ups. These studies showed the feasibility of SPH for multi-grain grinding simulation. The height distribution of abrasive grains and the workpiece surface geometry during grinding were not consider. Both were addressed in this study using SPH to predict the grinding force in RA.

In this study, the grinding wheel motion and contact with the surrogate of the hardened plaque in RA were measured by the high-speed camera and piezoelectric dynamometer, respectively. The ground surface was inspected under scanning electron and laser confocal microscopes. The discrete wheel-workpiece contact was observed due to the grinding wheel bouncing on the plaque surface. The impact force was estimated by Hertz contact law [10,11] and found to be the dominant component in RA grinding force.

The cutting force for plaque removal was studied by SPH modeling. Based on the wheel motion and abrasive grain geometry and distribution, a grinding wheel model with multiple grains was established to simulate the grinding process using the SPH modeling. In this model, the grinding zone of the workpiece was modeled in SPH particles. The rest of the workpiece and the grinding wheel with small deformation were modeled by the Lagrangian finite elements (LFE) to save computational time [2,4,9]. The workpiece surface geometry during grinding was modeled by kinematic-geometrical (K-G) model via a virtual grinding wheel [12]. The simulation predicted cutting force, together with the impact force, was compared with experimental measurements.

The experimental setup of RA to measure the grinding wheel motion, force, and ground surface geometry is first introduced. The discrete grinding and impact force calculation are then illustrated. SPH modeling of the RA grinding process, including the confocal scanning of the grain geometry and spacing, multi-grain wheel modeling, workpiece K-G modeling, and SPH simulation, is elaborated. Comparison of the grinding force results is presented, followed by a discussion on the clinical significance and the multi-grain modeling technique.

4.2 Experimental Investigation on RA Discrete Grinding Mechanism

Experiments were setup and conducted to investigate the grinding wheel motion, grinding force, and ground surface in RA.

4.2.1 Experimental setup

The experimental setup, as shown in Figure 4.2, consists of three modules: RA device, arterial phantom, and grinding wheel motion and force measurement system.

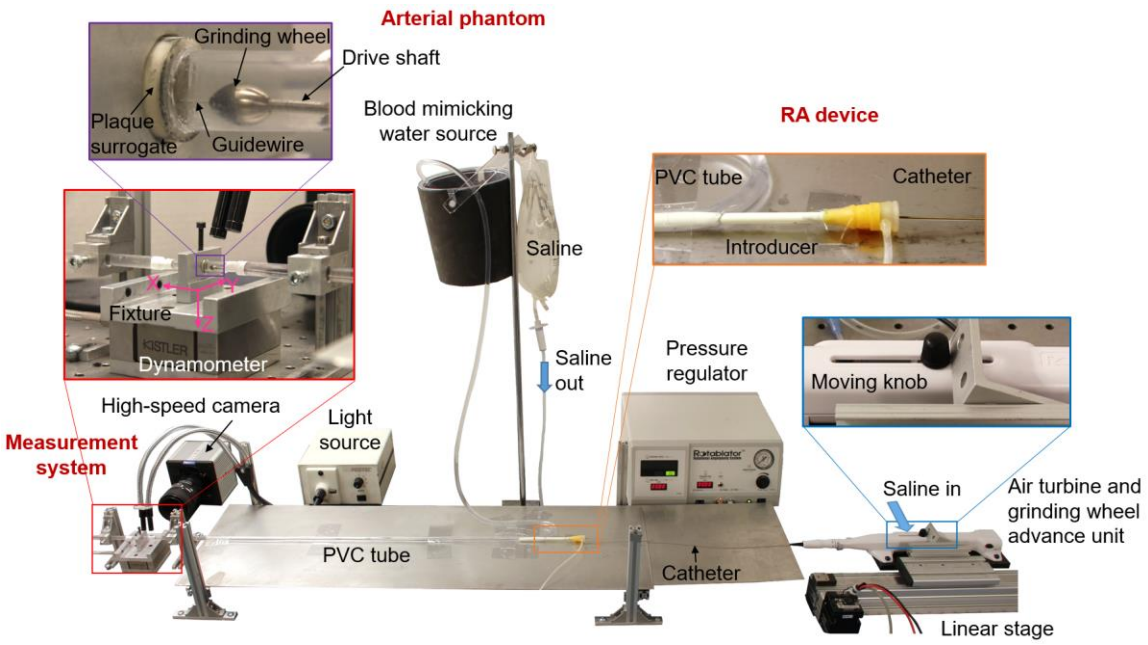

Figure 4.2 Experimental setup.

4.2.1.1 RA device

The RA device is the Rotablator™ by Boston Scientific (Marlborough, MA). This device consists of a catheter, an air turbine and grinding wheel advance unit, and an air pressure regulator. Catheter, as shown in Figure 4.3, is inserted into a patient's artery during RA. The catheter consists of a grinding wheel, a stainless steel guidewire (0.23 mm diameter), a drive shaft (0.65 mm outer diameter (OD) and 0.29 mm inner diameter (ID), and a sheath (1.43 mm OD, 1.03 mm ID). The stationary guidewire extends from the air turbine through the drive shaft and grinding wheel to beyond the plaque (Figure 4.1). The guidewire serves as a rail which the grinding wheel and drive shaft rotate around and translate along. Around the guidewire is the drive shaft as illustrated in the cross-section A-A in Figure 4.3. The drive shaft connects the grinding wheel and air turbine and is made of three helically wound 0.18 mm diameter stainless steel coils. The drive shaft rotates inside a stationary sheath made of polytetrafluoroethylene (PTFE). The friction between the rotational drive shaft and stationary guidewire and sheath is reduced by saline flowing between the sheath and guidewire during RA. The grinding wheel is a nickel plated brass prolate spheroid with the half distal to the drive shaft coated with diamond abrasive grains, as can be seen in the laser confocal scanning image in Figure 4.3. The maximum diameter

of the grinding wheel ranges from 1.25 to 2.5 mm. In this study, a 2.38 mm diameter grinding wheel was used.

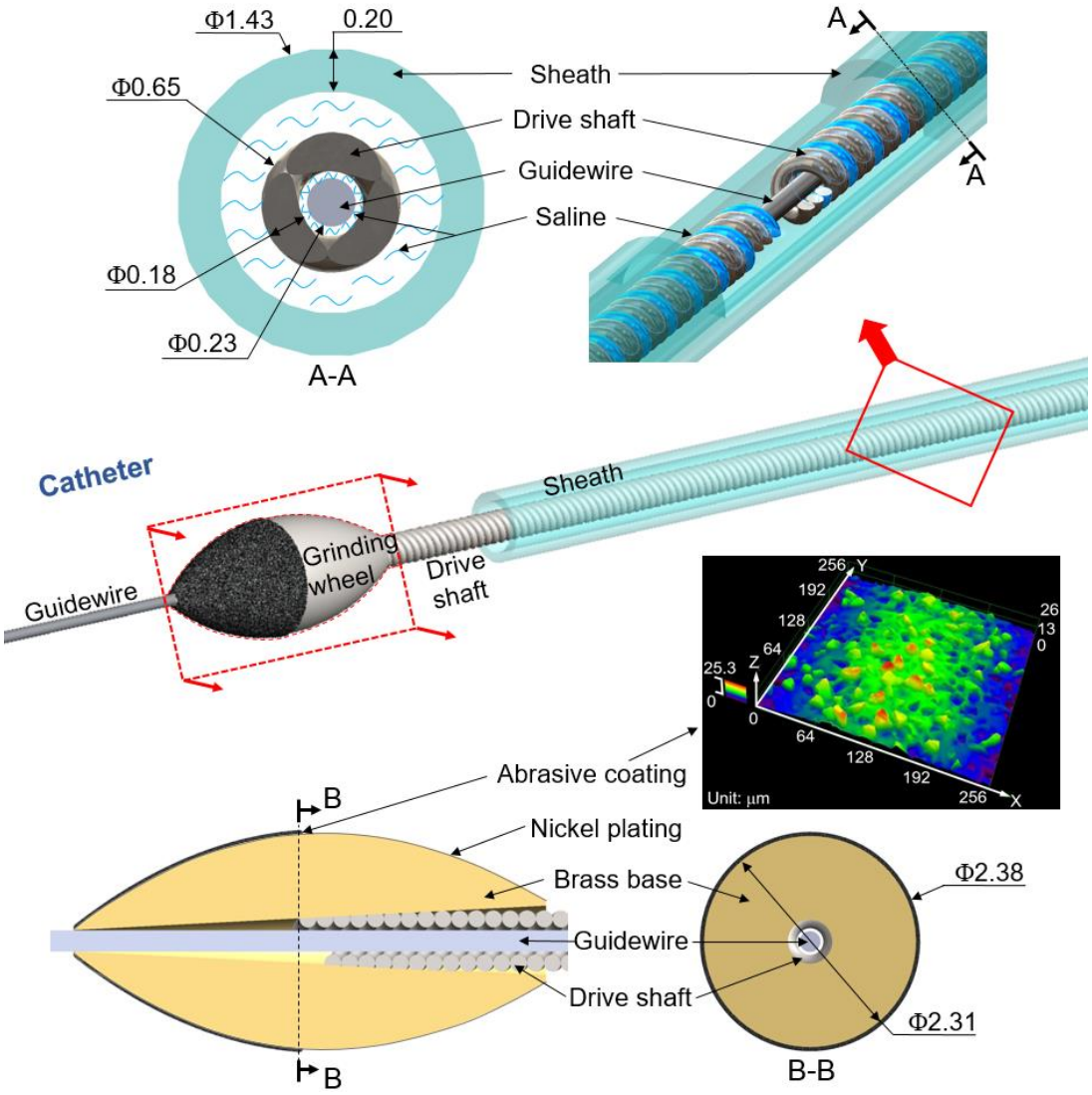

Figure 4.3 RA catheter components and dimensions. (unit: mm)

The air turbine drives the grinding wheel via the drive shaft from 6,000 to 230,000 rpm. An air pressure regulator sets the rotational speed of the grinding wheel. The grinding wheel translation on the guidewire is manually controlled by the moving knob during RA, as shown in Figure 4.2. In this experiment, the knob was moved by a linear stage (HLD60, Moog Animatics, Milpitas, CA) to control the wheel axial motion.

4.2.1.2 Arterial phantom

The arterial phantom, simulating the compliant artery environment in RA, consisted of a plaque surrogate, a PVC tube, and a blood mimicking water source. The surrogate for calcified plaque is an 8 mm long ring-shape bovine bone with 4 mm ID, mimicking a lesion in the coronary artery [13]. Inner surface of the bone surrogate was polished by an 800-grit size flexible cylinder hone to smooth the hole inner surface. Such polished surface is necessary to reveal the ground grooves during RA. This ring-shape bone was connected to the blood mimicking water source by a 1.5 m long PVC tube (9.53 mm OD and 1.59 mm thickness) with 37°C water flow through at 30 ml/min flow rate, which simulated the blood flow in coronary artery. The RA catheter was inserted to a PVC tube via the introducer (marked in Figure 4.2) to give the grinding wheel access to the plaque surrogate.

4.2.1.3 Measurement system

The plaque surrogate was mounted on the top of a piezoelectric dynamometer (Model 9256-C, Kistler, Winterthur, Switzerland) as shown in Figure 4.2. While grinding inside the plaque surrogate, the grinding force on the bone surrogate was measured by the dynamometer at 5,000 Hz sampling rate. A high-speed camera (FASTCAM-1024PCI, Photron, Tokyo, Japan) was used to record the RA catheter motion at 6,000 frames per second. Under such high frame rate, the bright and consistent lighting condition was necessary to obtain quality images. A fiber optic light source (Model 8375, Fostec, Ansan, Korea) was used to deliver a concentrated illumination.

4.2.1.4 Experiment design

The grinding wheel rotated at 135,000, 155,000 or 175,000 rpm and passed one-way through the bone surrogate at 6.7, 7.3, or 8.0 mm/s, respectively. Grinding force was measured and the catheter motion was recorded. Each test was repeated five times. After grinding, the surrogates were cut in halves for examination of ground surface.

4.2.2 Orbital speed

The grinding wheel orbital speeds (Ω) was calculated from the high-speed camera images. Detailed method has been introduced in a previous study [14]. At 135,000,

155,000, and 175,000 rpm rotational speed, the mean of orbital speeds were 6,168, 6,783, and 7,686 rpm with standard deviation of 63, 113, and 127 rpm, respectively. The orbital frequency was higher with the increased rotational speed. The standard deviations were small, less than 2% of the average, indicating the RA tests had good repeatability.

4.2.3 Grinding force

Figure 4.4 shows the grinding force at 135,000 rpm wheel rotational speed measured by the dynamometer Y-axis, $F_{G,Y}$. A cyclic pattern is observed due to the grinding wheel orbital motion [14]. The period of an orbital cycle in this example was 9.5 ms, corresponding to an orbital speed of 6,060 rpm which matched well with the 6,168 rpm measured using the high-speed camera. The wheel orbital speed was also identified by processing the measured force using the fast Fourier transform. At 135,000, 155,000, and 175,000 rpm wheel rotational speeds, the orbital speeds obtained from the measured force were 6,060, 6,840, and 7,800 rpm with standard deviations of 67, 89, and 72 rpm, respectively. These values agreed well with those observed by the high-speed camera method.

The average grinding force, F_G, as indicated by the dashed line in Figure 4.4, was calculated by averaging the maximum forces (marked in red circles) in consecutive windows of 10 orbital cycles. The average grinding forces were 1.84, 1.92, and 2.22 N with the standard deviations of 0.11, 0.04, and 0.01 N, at 135,000, 155,000, and 175,000 rpm grinding wheel rotational speed, respectively.

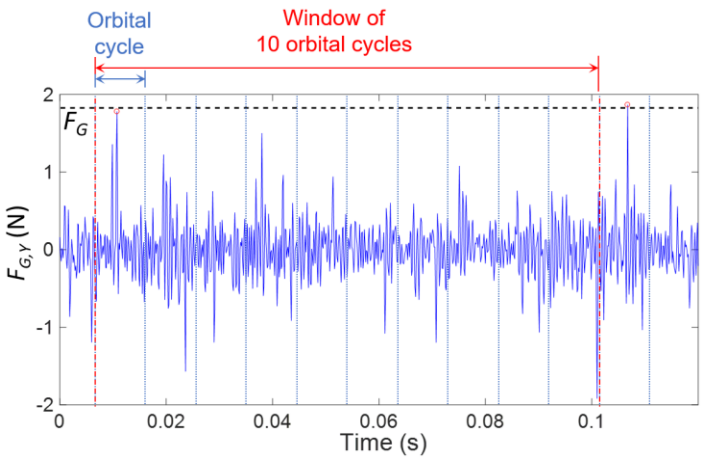

Figure 4.4 $F_{G,Y}$ measurement in orbital cycles and the averaged grinding force F_G.

4.2.4 Ground surface and discrete grinding

From the ground surface, the grinding wheel was observed to bounce on the wall while orbiting inside the bone surrogate in RA. As shown in Figure 4.5(a), the bone-made surrogate after RA grinding was cut in halves and examined under an environmental scanning electron microscopy (ESEM) (Quanta, FEI, Hillsboro, OR). For each bone specimen, five images were taken at 30° angle interval around the cylindrical axis and stitched together as shown in Figure 4.5(b). On the ground surface, separate spot scratches aligned in a line along the grinding wheel orbital path. This line repeated in the wheel advancing direction. This observation indicates the discrete grinding: while carried by the blood flow, the orbiting grinding wheel bounces on the bone surrogate surface and leaves discrete grinding marks along the path, as demonstrated in Figure 4.5(c).

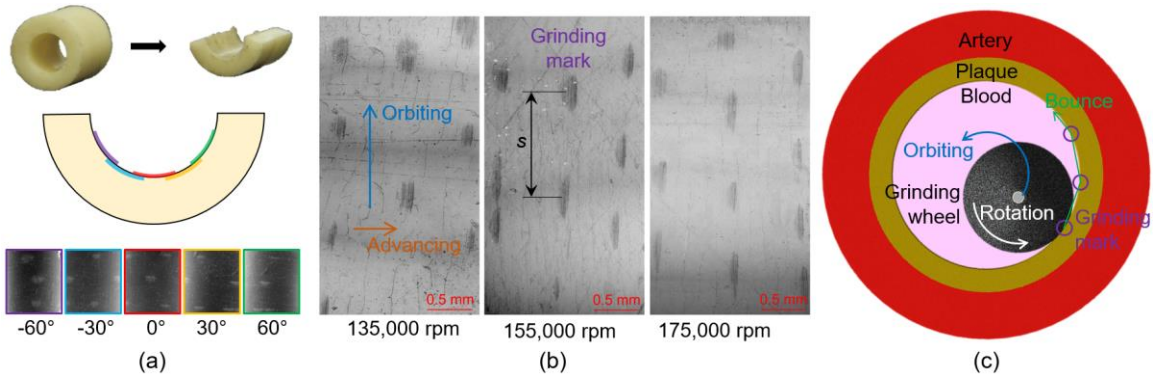

Figure 4.5 Ground surface (a) ESEM examination, (b) images at three grinding wheel rotational speeds, and (c) discrete grinding on bone surrogate in RA.

4.2.5 Individual grinding mark characterization

The individual grinding mark was observed using laser confocal microscope (LEXT OLS4000, Olympus, Tokyo, Japan) with a resolution of 10 nm in height and 120 nm in length and width. A sample image of a grinding site generated at a 135,000 rpm wheel rotational speed is shown in Figure 4.6. The depth of penetration, width, and length of a grinding mark were measured using the confocal microscopy on the inner surface of sectioned bone surrogate. For each rotational speed, nine grinding marks were examined. The average and standard deviation (std) of the depth of penetration, width, and length of the nine grinding marks are presented in Table 4.1 for the three investigated grinding wheel rotational speeds. The depth of penetration increased with the rotational speed. The width

and length were less affected by the wheel rotational speed, except that the length at 135,000 rpm was smaller than those at higher speeds. Variation of the ground surface geometry was large because the constraint of the grinding wheel orientation was weak due to the flexible drive shaft.

Table 4.1 Averaged depth of penetration, width, and length of nine grinding marks for three grinding wheel rotational speeds.

Rotational speed [rpm]	Depth of penetration [μm] average (std)	Width [μm] average (std)	Length [μm] average (std)
135,000	3.6 (0.8)	130 (56)	368 (55)
155,000	4.4 (1.2)	132 (51)	449 (55)
175,000	5.7 (1.2)	128 (33)	449 (65)

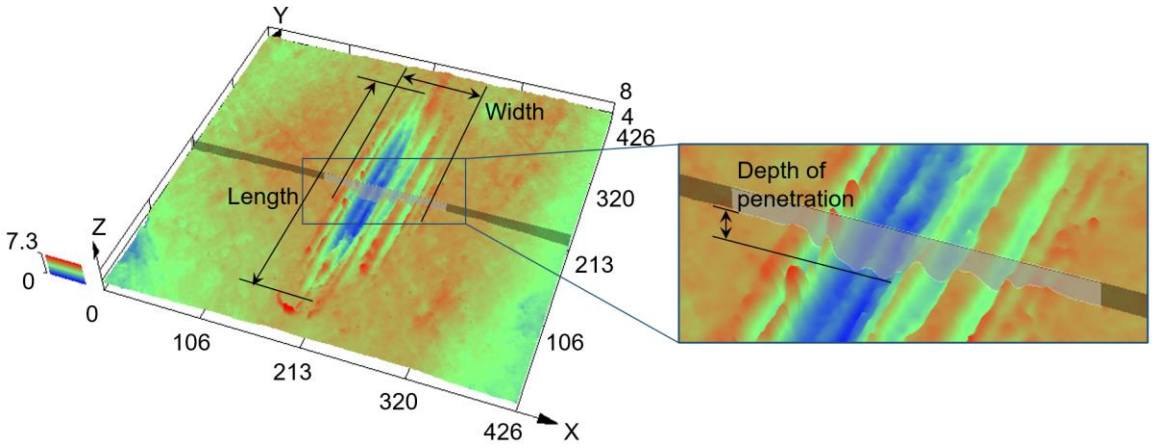

Figure 4.6 Laser confocal microscopy measurement of the depth of penetration, width, and length of a grinding mark. (unit: μm)

4.3 Bouncing Grinding Wheel and Impact Force

The bouncing grinding wheel and the discrete grinding mechanism (Figure 4.5(c)) are caused by the impact force during the contact between the grinding wheel and the bone surrogate. Based on the grinding wheel kinematics and Hertz contact model, the impact force can be calculated.

4.3.1 Grinding wheel kinematics and force analysis

The grinding wheel kinematics and force analysis are illustrated in Figure 4.7. O_w and O_s are the centers of the vessel lumen (with a radius of R = 2 mm) and the grinding wheel (with a radius of r = 1.19 mm), respectively. G is the contact point between the grinding wheel and the bone. As shown in Figure 4.7(a), after the contact (and grinding) at G, the center of the grinding wheel moves with velocity $\boldsymbol{v_s}$ from O_s to O_s' and the wheel surface hits G'. Due to the collision at G', the grinding wheel changes the velocity to $\boldsymbol{v_s}$' and its center moves towards O_s" and surface hits G". We assumed a linear motion of the grinding wheel between two contact points, due to the small hydraulic force ($F_{H,t}$, $F_{H,n}$) on the grinding wheel [15], as illustrated in Figure 4.7(b). The distance between two

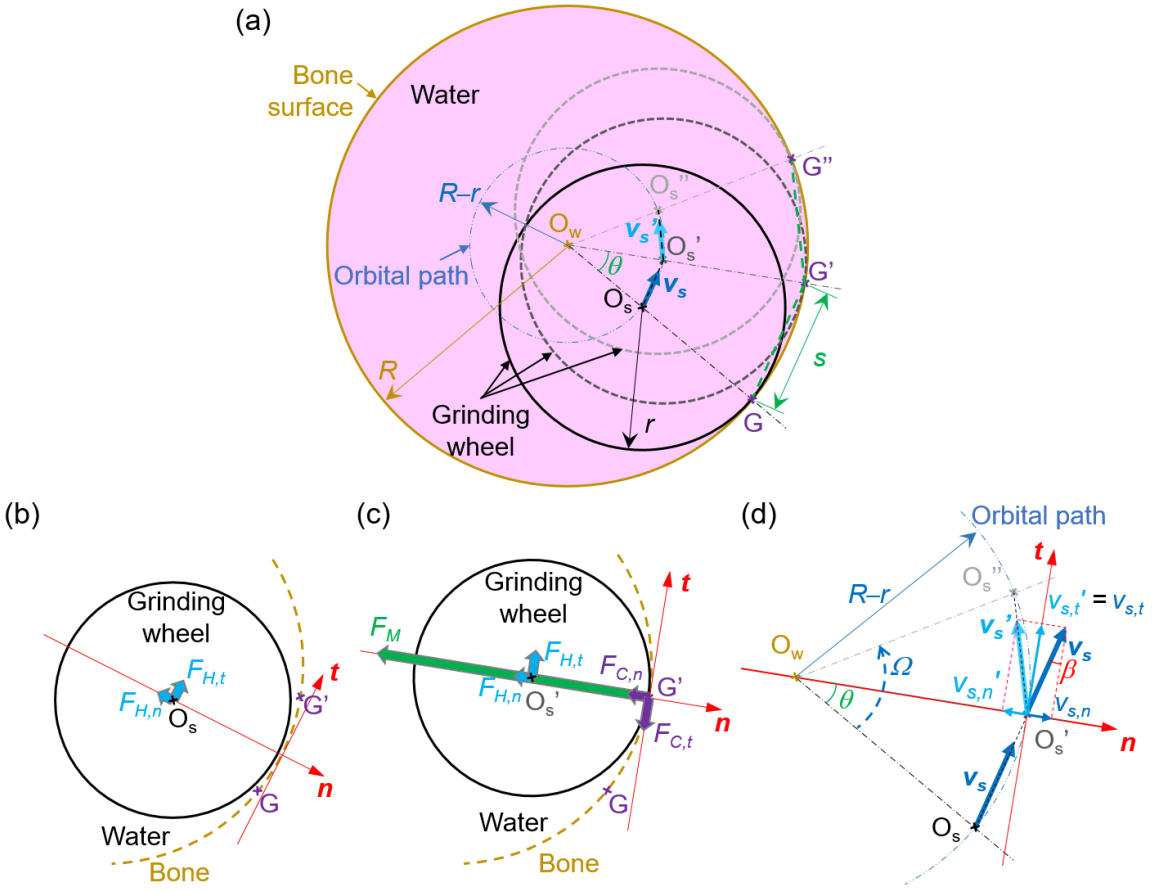

Figure 4.7 Dynamics of the grinding wheel in three contact positions in RA discrete grinding: (a) kinematics configuration, (b) hydraulic force on the wheel between two contact points, (c) impact, hydraulic, and cutting forces at contact, and (d) the change of velocity of the grinding wheel during impact.

consecutive contact points (e.g. G and G') is denoted as *s*, which can be measured on ESEM images (Figure 4.5(b)). In this study, the average *s* was 1.04, 0.95, and 0.86 mm for 135,000, 155,000, and 175,000 rpm grinding wheel rotational speed, respectively.

During the contact with the bone surrogate, the grinding wheel is subject to three forces, as shown in Figure 4.7(c), the impact force $\boldsymbol{F_M}$, the cutting force $\boldsymbol{F_C}$, and the hydraulic force $\boldsymbol{F_H}$. $\boldsymbol{F_M}$ changes the grinding wheel velocity component normal to the contact surface change from $v_{s,n}$ to $v_{s,n}'$, as shown in Figure 4.7(d). $v_{s,n} = v_s \sin\beta$ where $v_s \approx \Omega(R-r)$ and $\beta = \theta/2 \approx s/(R-r)/2$. Based on the measured Ω and *s* at 135,000, 155,000 and, 175,000 rpm grinding wheel rotational speed, $v_{s,n}$= 0.133, 0.137, and 0.142 m/s, respectively, in this study.

4.3.2 Impact force

Based on the Hertz contact model [10,11], the impact force $\boldsymbol{F_M}$ can be expressed as:

$$F_M = K\delta^{1.5} \tag{4.1}$$

where *K* is a generalized stiffness parameter and δ is the displacement of grinding wheel during colliding with the bone surrogate due to elastic deformation. *K* depends on the radii of curvature of two contact surfaces and the elastic modulus and Poisson's ratio of two materials in contact [11]:

$$K = \frac{4\sqrt{R_E}}{3(\sigma_B + \sigma_G)} \tag{4.2}$$

$$R_E = (r^{-1} - R^{-1})^{-1}, \quad \sigma_B = \frac{1-{\nu_B}^2}{E_B}, \quad \sigma_G = \frac{1-{\nu_G}^2}{E_G}$$

where R_E is the effective contact curvature, σ_B and σ_G are the material parameters of the bone surrogate and the grinding wheel, respectively. E_B, ν_B, E_G, ν_G are the elastic modulus and Poisson's ratio of the bone surrogate and the grinding wheel, respectively. In this study,

the bovine bone surrogate has E_B= 18 GPa and ν_B = 0.30 [16], the brass grinding wheel has E_G= 105 GPa and ν_G = 0.31, and hence K=1.22×10^9 N/m$^{1.5}$.

The impact force can also be calculated based on Newton's second law on the grinding wheel:

$$F_M = m\frac{d^2\delta}{dt^2} \tag{4.3}$$

and substituting $\boldsymbol{F_M}$ by Eq. (4.1), we have an differential equation about δ:

$$K\delta^{1.5} = m\frac{d^2\delta}{dt^2} \tag{4.4}$$

where the mass of the grinding wheel, m, is 0.11 g. Eq. (4.4) was solved by MATLAB (v2016a, MathWorks, Natick, MA) ODE45 solver with the initial conditions: $\delta = 0$ and $\frac{d\delta}{dt} = v_{s,n}$ at t = 0, in a time span (0, t_n). At t_n, $\delta = 0$ and $\frac{d\delta}{dt} = -v_{s,n}$, the grinding wheel is about to leave the bone surface. F_M can be calculated using Eq. (4.1). Figure 4.8 shows $\boldsymbol{F_M}$ change over time during the collision at three investigated grinding wheel rotational speeds. The maximum $\boldsymbol{F_M}$ during collision was 1.84, 1.91, and 2.00 N for 135,000, 155,000, and 175,000 rpm rotational speed, respectively.

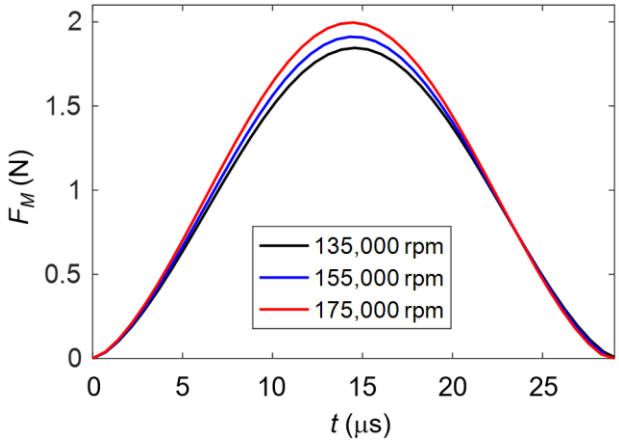

Figure 4.8 Impact force at different grinding wheel rotational speeds.

4.4 SPH Modeling of RA Cutting Force

The SPH model was established to estimate the cutting force $\boldsymbol{F_C}$. The SPH simulation of the RA material removal process was carried out in LS-DYNA (R8.1.0, LSTC, Livermore, CA) using the massively parallel processing mode on six compute nodes, each configured with two eight-core processors.

4.4.1 Kinematic and geometrical configuration of the SPH simulation

An overview of the SPH model with parameters based on the experiment setup is shown in Figure 4.9. Figure 4.9(a) shows the grinding wheel rotated around its axis (O_s)

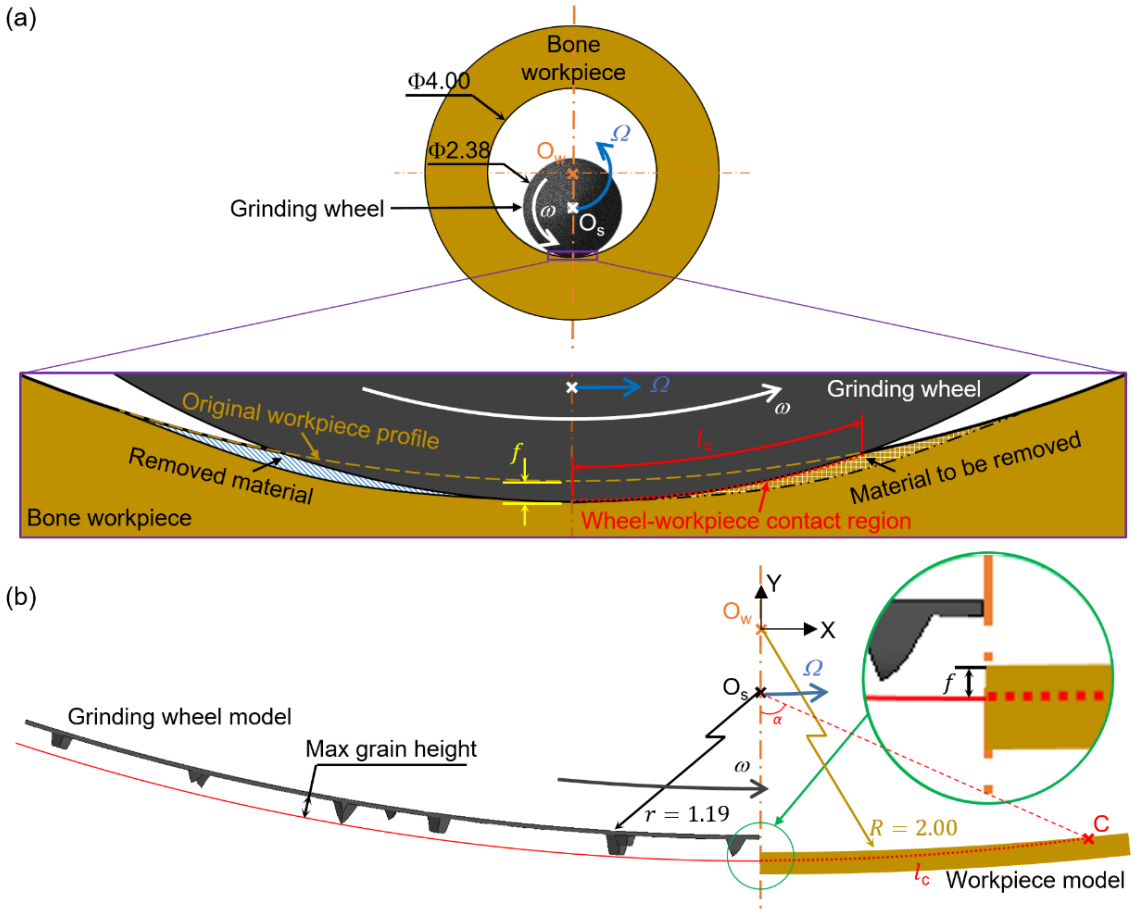

Figure 4.9 SPH simulation model (a) geometrical configuration and (b) close-up view of the grinding wheel model with abrasive grains and depth of penetration *f*. (unit: mm)

at a rotational speed of ω, orbited inside the bone surrogate with center axis (O_w) at an orbital speed of Ω, and cut the workpiece with the depth of penetration of f. Close-up view of the configuration of the abrasive grains on the grinding wheel (2.38 mm OD) contacting with the workpiece (4.0 mm ID) is shown in Figure 4.9(b). In this configuration, the highest grain in the grinding wheel would cut the workpiece with a depth of f in the simulation. The wheel-workpiece contact region is marked by the red dotted curve in Figure 4.9(a). The contact arc length l_c can be calculated using the following equation:

$$l_c = (r+f)\tan^{-1}\frac{\sqrt{4R^2f^2+8R^2rf-4Rrf^2-8Rr^2f-4r^2f^2-4rf^3-f^4}}{2Rr-2r^2-2rf-f^2} \quad (4.5)$$

Derivation of Eq. (4.5) is presented in Appendix I.

Three cases of SPH simulation, marked as Cases 1, 2, and 3 with the grinding wheel rotational and orbital speeds, depth of penetration, and contact arc length summarized in Table 4.2, were conducted with f equal to the experimentally measured depth of penetration.

Table 4.2 Kinematic and geometrical parameters in three SPH simulation cases.

Case	Rotational speed, ω [rpm]	Orbital speed, Ω [rpm]	Depth of penetration, f [μm]	Contact arc length, l_c [μm]
1	135,000	6,060	3.6	145
2	155,000	6,840	4.4	161
3	175,000	7,800	5.7	184

4.4.2 Multi-grain grinding wheel geometrical modeling

4.4.2.1. Grain geometry

Topography of the abrasive surface on the grinding wheel was measured using the same laser confocal microscope in Section 4.2.5 for the ground surface. Measurement of the grinding wheel abrasive surface is shown in Figure 4.10(a). Two types of grain tip were observed: the flat- and point-tip, as marked by F and P in Figure 4.10(b), respectively. The number of the flat- and point-tip grains were roughly the same, with a ratio of 23:27

in 100 examined sample grains. The flat- and point-tip grains were modeled as a truncated square pyramid (Figure 4.10(c)) and a triangular pyramid (Figure 4.10(d)), respectively. Dimensions of the grain models were estimated by summarizing 10 grains of each type.

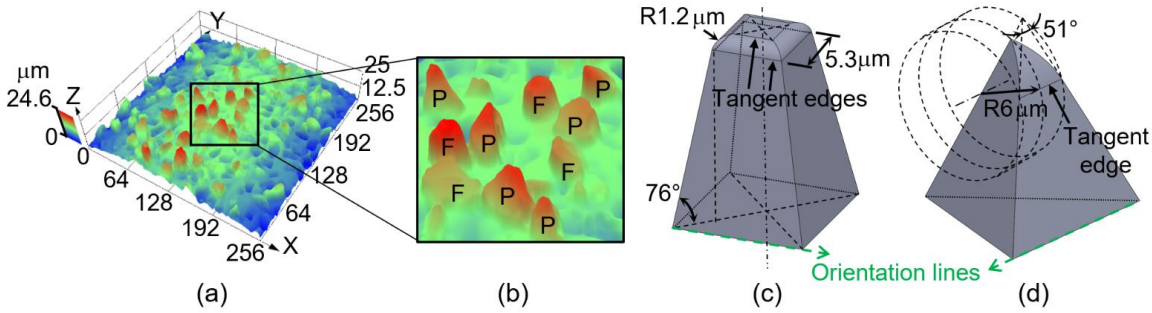

Figure 4.10 Abrasive grain modeling: (a) grinding wheel surface image, (b) flat- and point-tip grains, and models and dimensions of (c) flat- and (d) point-tip grains.

4.4.2.2 Grain distribution

Three 256 μm × 256 μm measurement areas on the surface of the grinding wheel around the 2.38 mm maximum OD region were measured using the confocal microscope. An effective surface area of 190,617 μm^2 and 232 grains was identified. The height from the tip of the grain to the base surface (designed with zero height) was measured. The height distribution of the 232 grains, ranging from 0.6 to 10.5 μm, is shown in Figure 4.11(a). Based on the largest 5.7 μm depth of penetration (in Case 3), grains lower than 4.8 μm (= 10.5 – 5.7 μm) were not cutting into the workpiece and therefore inactive. Considering potential workpiece surface variation during cutting (debris build-up on the surface), a buffer distance of 0.3 μm was added to designate active grains with a height between 4.5 to 10.5 μm. In this range, a total of 113 active grains were identified.

The grinding wheel model, as shown in Figure 4.11(b) to (e), had 9 active grains (4 flat-tip and 5 point-tip) to represent the active abrasive grains. This grinding wheel model was a segment of the cylindrical surface with an arc length of 370 μm, which was twice of the wheel-workpiece contact arc length (l_c in Figure 4.9(a)) in Case 3 (the longest l_c among three Cases). The width was 41 μm, which was calculated based on the surface area (15,181 μm^2) for 9 active grains in the effective surface area measured by confocal microscope (190,617 μm^2 for 113 active grains). Within this stripe, the position and

orientation of the 9 active grains were allocated randomly. A 3-by-9 uniformly distributed random number matrix were applied to assign the location and orientation of these 9 active grains. Results are shown in Figures. 4.11(c) and (d). The maximum height of the active grain was 10.5 μm. Heights of remaining 8 grains were determined by dividing the 130 remaining active grains in descending order into 8 groups based on height. The average heights of these 8 groups were 10.0, 8.6, 7.7, 7.0, 6.4, 5.7, 5.3, and 4.7 μm. These with the 10.5 μm maximum height were assigned randomly to the 9 active grains in the model, as shown in Figure 4.11(b).

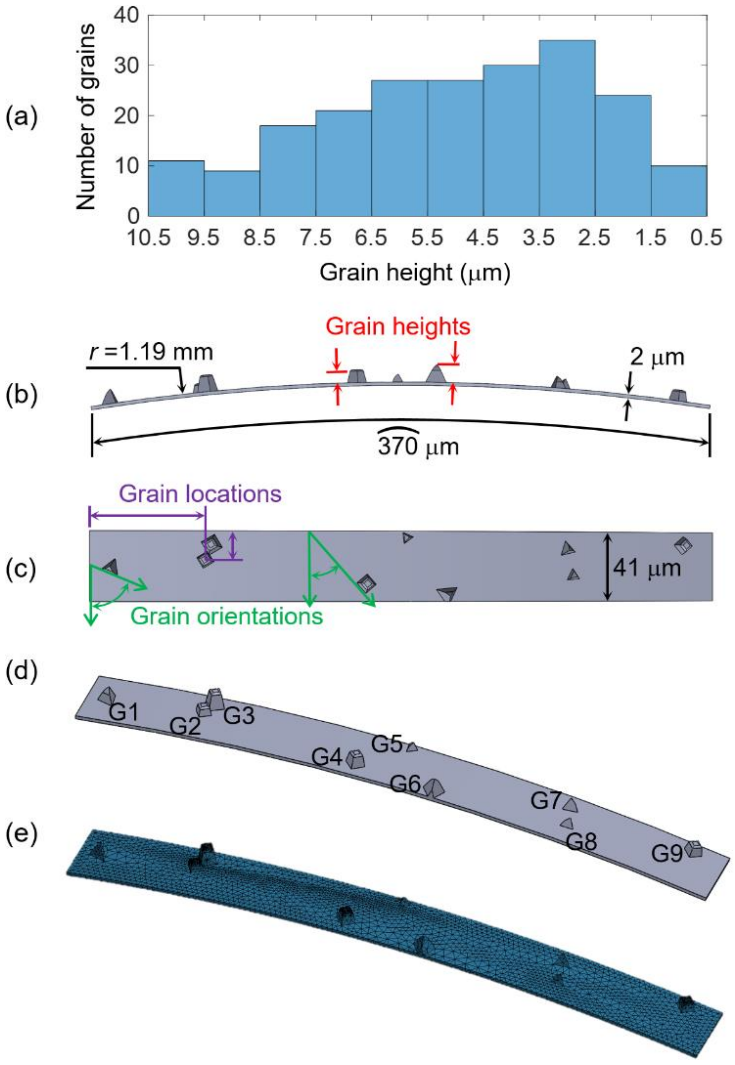

Figure 4.11 Grinding wheel modeling: (a) height distribution of all measured grains, the (b) front, (c) top, and (d) 3D view of the grinding wheel model, and the (e) meshed model.

The grinding wheel model was meshed by 12,725 tetrahedron elements using ANSYS (v16.1, ANSYS, Canonsburg, PA), as shown in Figure 4.11(e). The grinding wheel was modeled as a rigid body due to its high elastic modulus in comparison to the bone work-material.

4.4.3 Workpiece modeling

Modeling of the workpiece consisted of three steps. First, a segment of the cylindrical wall of the grinding zone in the workpiece was established. Second, the segment was divided for the SPH and LFE modeling. Third, this segment was modified by geometrical-kinematic modeling to prepare the workpiece surface for SPH simulation.

4.4.3.1 Workpiece shape and dimension

As shown in Figure 4.12(a), the workpiece model was a 41 μm wide (match to the grinding wheel width in Figure 4.11(c)) cylindrical wall with an inner surface radius of R = 2 mm, a thickness of d, and an arc length of l_w. The d and l_w varied in three cases due to different f and contact arc length l_c.

The thickness of the workpiece d = 10.6, 11.4, and 12.7 μm for Cases 1, 2, and 3, respectively, based on the f in Table 4.2 and a buffer thickness of 7 μm.

The arc length of grinding zone l_w is equal to the sum of l_o, l_c, and an additional 3 μm buffer distance. The wheel orbital distance, l_o, can be calculated by:

$$l_o = (R + f)\Omega t \tag{4.6}$$

where t is the time duration of the grains traveling a distance twice of l_c.

$$t = \frac{2l_c}{(r + f)\omega} \tag{4.7}$$

In Cases 1, 2, and 3, t = 17.2, 16.6, and 16.8 μs, l_o = 19, 14, and 17 μm, respectively. Adding the l_c in Table 4.2 and the 3 μm buffer distance, l_w = 167, 178, and 204 μm in Cases 1, 2, and 3, respectively.

4.4.3.2. SPH particle and LFE mesh

Three regions in the workpiece were modeled. As shown in Figure 4.12(b), the top grinding zone was modeled using SPH particles. The bottom 1 μm layer had negligible deformation and was modeled as a rigid body and meshed by tetrahedron LFEs. The region in between the particles and the rigid elements was meshed with deformable hexahedron LFEs.

SPH particle size in this model was 0.4 μm. A particle size independent study was conducted via a single grain scribing study. The 1.6, 0.8, and 0.4 μm SPH particles were applied to model a 10×10×50 μm cuboid workpiece which was scribed by a flat-tip grain across the top surface of the workpiece with a 5 μm depth of cut and 23 m/s cutting speed (the grinding wheel surface speed in Case 3). The L2 relative error norm of the scribing force was less than 10% between the 0.4 and 0.8 μm SPH particle size.

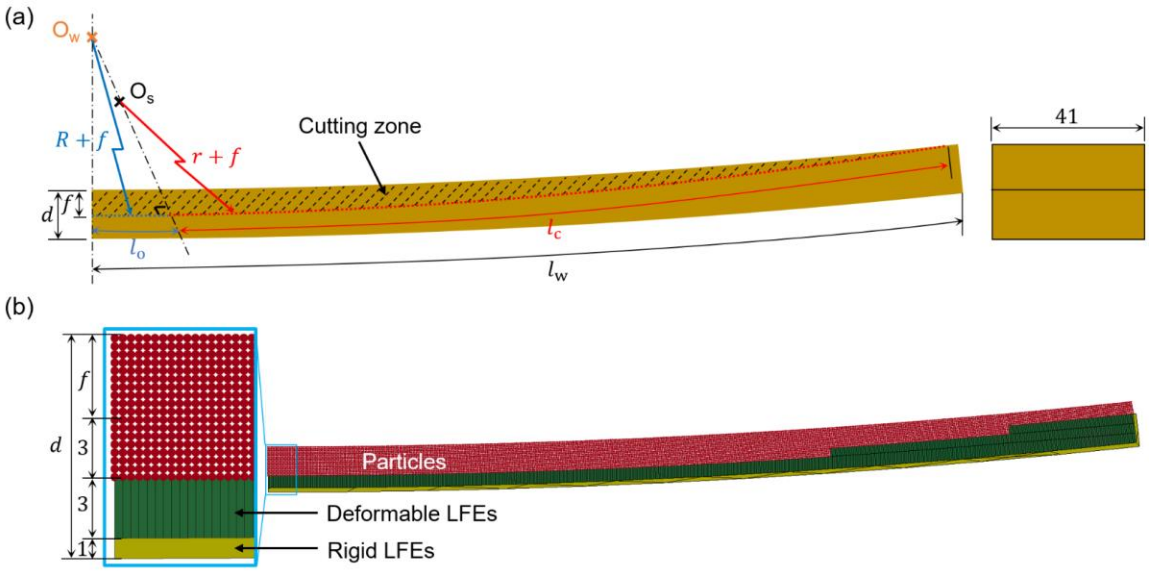

Figure 4.12 Workpiece modeling: (a) workpiece dimensions and cutting zone and (b) three workpiece regions with a top layer of 0.4 μm SPH particles and bottom two LFE layers. (unit: μm)

4.4.3.3 Kinematic-geometrical (K-G) cutting of the workpiece surface

The top workpiece surface was modified by the kinematic-geometrical (K-G) cutting, which, as shown in Figure 4.13(a), used a grinding wheel model with abrasive tip geometry to sweep across the workpiece surface, removed all SPH particles in contact, and

created a rough and realistic surface topography for the SPH simulation to predict the cutting force. The grinding wheel model in Figure 4.13(a) had the same width (41 μm). The 113 active grains in 190,617 μm^2 area in the confocal microscopy measurement in Section 4.4.2.2, were rearranged in a 4,650 μm long and 41 μm wide cylindrical strip to be the grinding wheel model. The K-G cutting was performed in MATLAB by deleting SPH particles in contact with active grains during the grinding wheel model traveling from Figure 4.13(a) to (b) which was the SPH simulation starting configuration (Figure 4.9). Grain trajectories were calculated based on the grinding wheel kinematics (ω, Ω, and f).

For example, the surface generated from the K-G modeling for Case 3 is shown in Figure 4.13(c). The cross-sections A-A and B-B show the material removal along and across the active grain cutting direction in the workpiece after the K-G cutting. This was the surface of the SPH model that engaged with the grinding wheel model in Figure 4.11(e).

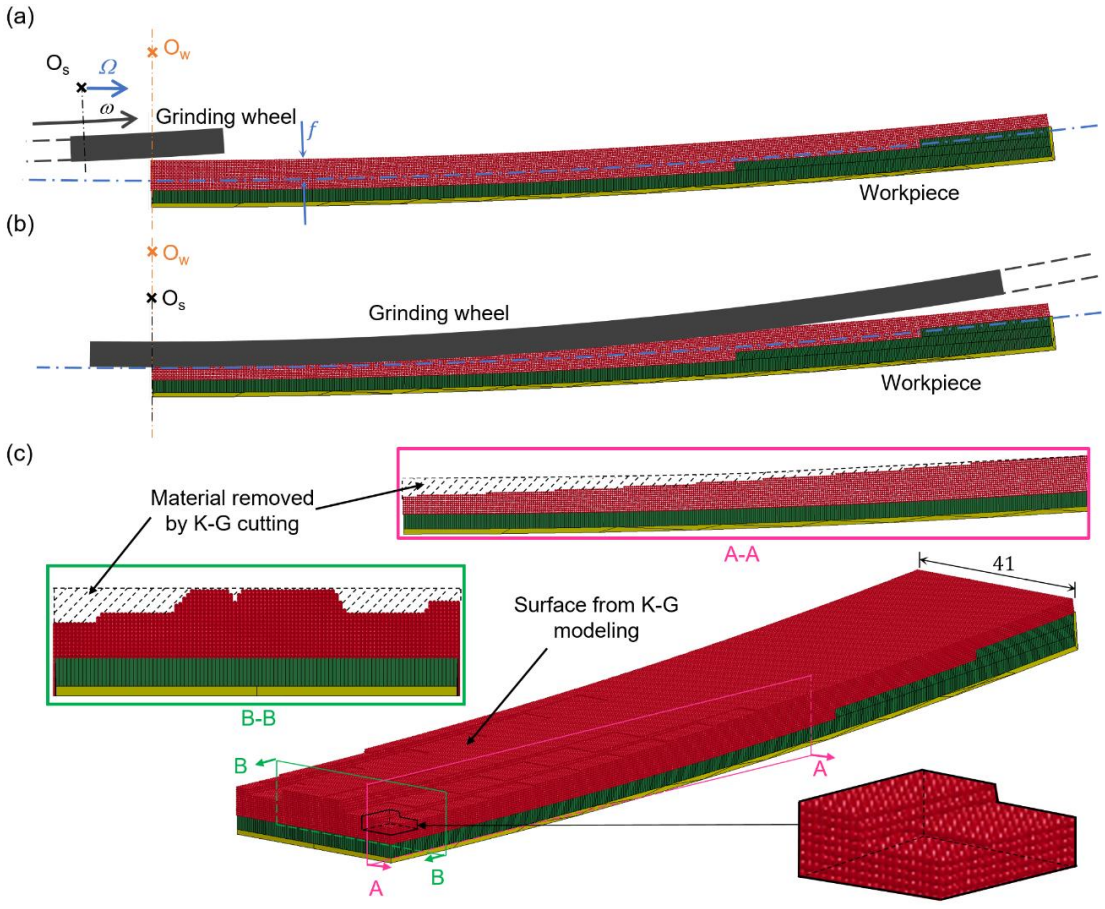

Figure 4.13 Kinematic-geometrical cutting of the workpiece: (a) starting and (b) ending configurations and (c) surface after K-G cutting.

4.4.4 Material property

The grinding wheel was assigned with the material property of 3,520 kg/m^3 density, 1,220 GPa elastic modulus, and 0.25 Poisson's ratio for the diamond active grain. The work-material properties included the stress-strain power law curves at 0.00167 to 250 s^{-1} strain rates from bovine bone tensile tests which were adopted from the experimental results by Crowninshield *et al* [17].

4.4.5 Cutting force calculation

Cutting force from the SPH simulation was scaled up by a ratio of the width of grinding (presented in Figure 4.6 and Table 4.1) and the 41 μm grinding wheel model. For Cases 1, 2, and 3, the ratio was 3.1, 3.1, and 3.0, respectively.

4.4.6 SPH simulation results

Figure 4.14 shows the cutting force and engagement of 9 active grains over time in Case 3 SPH simulation. The cutting force F_C and its tangential and normal components ($F_{C,t}$ and $F_{C,n}$) are shown in Figure 4.14(a). The peak cutting force is marked the circle. The peak cutting forces from the SPH simulation were 41, 51, and 99 mN for Cases 1, 2, and 3, respectively.

This multi-grain SPH model was able to simulate the interaction between each grain and the workpiece. As shown in Figure 4.14(b), the time period of each active grain (numbered from G1 to G9) engaging with the workpiece was marked by the bar graph. For example, the G3 cut the workpiece simultaneously with G1 and G2. The maximum force occurred when G6 started cutting with G3 and G4. This was also the time instance when the depth of cut was large.

Surface evolution and effect on the grain depth of cut were observed in this SPH simulation. The distribution of the von-Mises (v-m) stress in the bone surrogate and the active grains at five time instances in the SPH simulation were shown in Figure 4.14(c). G5, G7, and G9 were not engaged with the workpiece, as shown in Figure 4.14(b), mainly due to the trajectories of these grains overlapped with the groove cut by G2. This phenomenon can be observed in Figure 4.14(c).

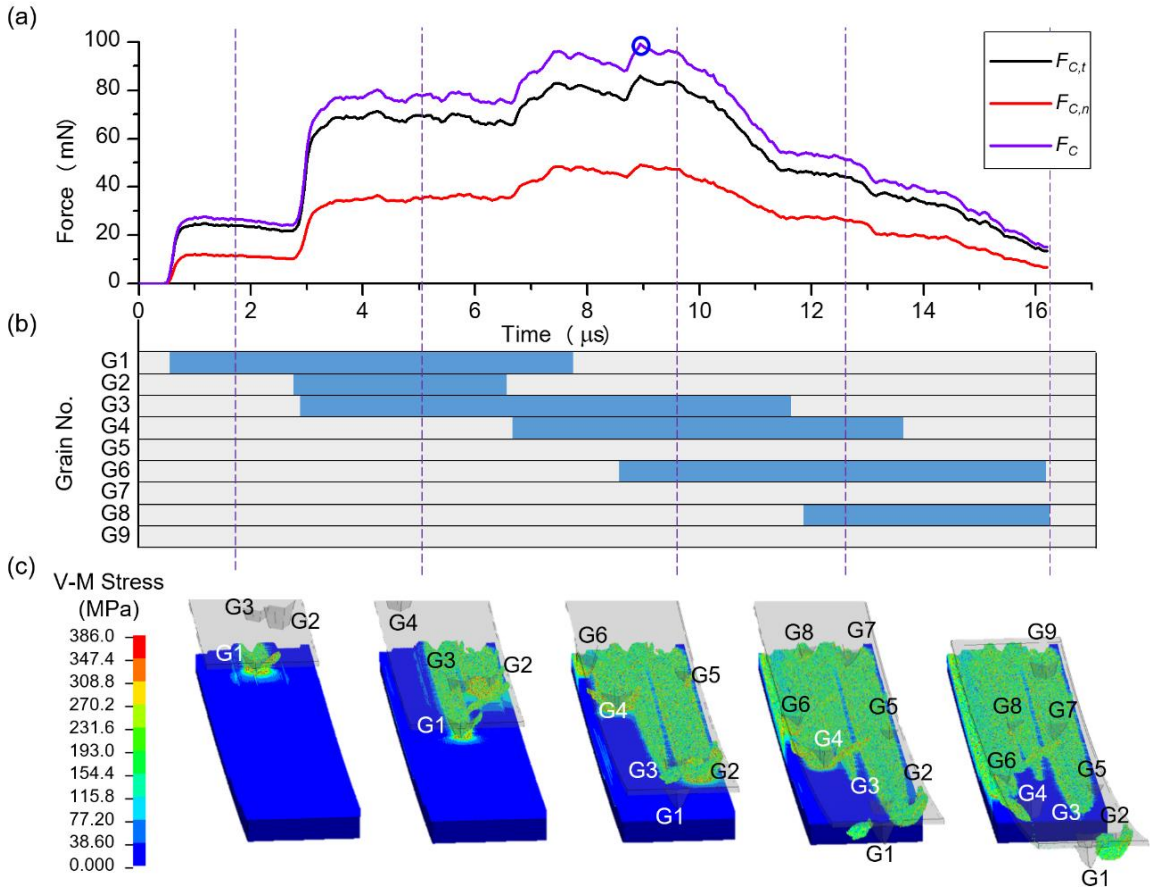

Figure 4.14 Cutting force and grain engagement in Case 3 SPH simulation: (a) cutting force and its normal and tangential components, (b) grain engagement time span, and (c) the von-Mises stress in five time instances.

To examine the grain location and orientation effect on the grinding force, another two grinding wheel models with randomized grain location and orientation were created and used in Case 3 SPH simulation. The peak grinding force simulated using these two grinding wheel models had 4.5% and 15.8% deviation from the Case 3 result in Figure 4.14(a). This shows that the SPH-predicted cutting force is not sensitive to the randomized grain location and orientation.

4.5 Discussions

4.5.1 Comparison of resultant grinding force

Based on Figure 4.7(c), the resultant grinding force F_G can be calculated as $((F_M+F_{C,n})^2 + F_{C,t}^2)^{0.5}$. Based on results of the impact force F_M in Section 4.3.2 and the cutting force ($F_{C,n}$, $F_{C,t}$) in Section 4.4.6, the model-predicted resultant grinding force is compared with the experimental measured grinding force (Section 4.2.3) in Table 4.3. The relative errors are smaller than 2% in Cases 1 and 2. In Case 3, the relative error is –7.7% which may be caused by a lack of consideration of the bone material hardening at a higher strain rate at 175,000 rpm grinding wheel rotational speed.

Table 4.3 Comparison of the RA grinding force modeling.

Case	Rotational speed (rpm)	F_M (N)	$F_{C,n}$ (mN)	$F_{C,t}$ (mN)	Model predicted F_G (N)	Experimental measured F_G (N)	Error (%)
1	135,000	1.84	21.5	35.5	1.86	1.84	1.1
2	155,000	1.91	25.5	44.7	1.94	1.92	1.0
3	175,000	2.00	49.2	86.1	2.05	2.22	-7.7

4.5.2 Clinical significance

Grinding force in RA is critical to the procedure safety and efficacy. Excessive grinding force may lead to vessel dissection and spasm. The RA grinding force increases with the grinding wheel rotational speed, and the grinding wheel bounces on the vessel wall while orbiting. The impact force in the radial direction of the vessel is the dominant force during RA. This impact force may help to disrupt the calcified plaque inner structure and reduce the lesion stiffness due to the plaque stress softening effect [18-21]. The cutting force for plaque removal is relatively small, as shown in Table 4.3. The cutting force increases with the rotational speed. A lower grinding wheel rotational speed in RA helps to avoid vessel dissection, however, may increase the debris size which will be further investigated.

4.6 Concluding Remarks

This study experimentally measured and developed a model to predict the grinding force in RA. The grinding force consisted of the impact and cutting forces, which were solved using Hertz contact and multi-grain SPH modeling approach, respectively. This RA grinding force model could facilitate better understanding the RA mechanism of action and improving the RA device design and clinical techniques.

This study has a few limitations. A ring-shape bovine bone was used as the surrogate to the calcified plaque. Future study on the effect of the irregular shape of the lesion and various surrogate materials to represent the calcified plaque is required. The debris formation and plaque disruption in RA also need further investigation.

References

[1] Rüttimann N, Roethlin M, Buhl S, Wegener K. Simulation of hexa-octahedral diamond grain cutting tests using the SPH method. Procedia CIRP. 2013;8:322-7.

[2] Shen RD, Wang XM, Yang CH. Numerical simulation of high speed single-grain cutting using a coupled FE-SPH approach. Appl Mech Mater. 2014;483:3-8.

[3] Cao J, Wu Y, Li J, Zhang Q. Study on the material removal process in ultrasonic-assisted grinding of SiC ceramics using smooth particle hydrodynamic (SPH) method. Int J Adv Manuf Tech. 2016;83(5):985-94.

[4] Su C, Ding JM, Zhu LD. Simulation research on cutting process of single abrasive grain based on FEM and SPH method. Adv Mat Res. 2011;186:353-7.

[5] Liu Y, Li B, Wu C, Zheng Y. Simulation-based evaluation of surface micro-cracks and fracture toughness in high-speed grinding of silicon carbide ceramics. Int J Adv Manuf Tech. 2016;86(1):799-08

[6] Zhang XL, Yao B, Feng W, Shen ZH, Wang MM. Modeling of a virtual grinding wheel based on random distribution of multi-grains and simulation of machine-process interaction. Journal of Zhejiang University Science. 2015;16(11):874-84

[7] Eder SJ, Cihak-Bayr U, Pauschitz A. Nanotribological simulations of multi-grit polishing and grinding. Wear. 2015;340:25-30.

[8] Ruttimann N, Buhl S; Wegener K. Simulation of single grain cutting using SPH method. J Mach Eng. 2010;10(3):17-29

[9] Shen RD, Wang XM, Yang CH. Coupled FE-SPH simulation of a high-speed grinding process using a multiple-grain model. Adv Mat Res. 2014;989:3248-51.

[10] Hertz H. Über die Berührung fester elastischer Körper. J reine und angewandte Mathematik. 1881;92:156–171.

[11] Flores P, Lankarani HM. Contact force models for multibody dynamics. New York: Springer International Publishing; 2016. 19 p.

[12] Brinksmeier E, Aurich JC, Govekar E, Heinzel C, Hoffmeister HW, Klocke F, *et al*. Advances in modeling and simulation of grinding processes. CIRP Ann-Manuf Techn. 2006;55(2):667-96.

[13] Dodge JT, Brown BG, Bolson EL, Dodge HT. Lumen diameter of normal human coronary arteries. Influence of age, sex, anatomic variation, and left ventricular hypertrophy or dilation. Circulation. 1992;86(1):232-46.

[14] Shih AJ, Liu Y, Zheng Y. Grinding wheel motion, force, temperature, and material removal in rotational atherectomy of calcified plaque. CIRP Ann-Manuf Techn. 2016;65:345-8.

[15] Zheng Y, Liu Y, Pitre JJ, Bull JL, Gurm HS, Shih AJ. Computational fluid dynamics modeling of the burr orbital motion in rotational atherectomy.

[16] Szabó ME, Taylor M, Thurner PJ. Mechanical properties of single bovine trabeculae are unaffected by strain rate. J Biomech. 2011;44(5):962-7.

[17] Crowninshield RD, Pope MH. The response of compact bone in tension at various strain rates. Ann Biomed Eng. 1974;2(2):217-25.

[18] Maher E, Creane A, Sultan S, Hynes N, Lally C, Kelly DJ. Inelasticity of human carotid atherosclerotic plaque. Ann Biomed Eng. 2011;39(9):2445-55.

[19] Walsh MT, Cunnane EM, Mulvihill JJ, Akyildiz AC, Gijsen FJ, Holzapfel GA. Uniaxial tensile testing approaches for characterisation of atherosclerotic plaques. J Biomech. 2014;47(4):793-804.

[20] Peña E, Peña JA, Doblaré M. On the mullins effect and hysteresis of fibered biological materials: a comparison between continuous and discontinuous damage models. Int J Solids Struct. 2009;46(7):1727-35.

[21] Maher E, Creane A, Lally C, Kelly DJ. An anisotropic inelastic constitutive model to describe stress softening and permanent deformation in arterial tissue. J Mech Behav Biomed Mater. 2012;12:9-19.

CHAPTER 5
CONCLUSIONS AND FUTURE WORK

5.1 Conclusions and Major Contributions

This dissertation studied the grinding wheel motion and associated hydraulic and grinding forces during plaque removal in arteries by atherectomy. Experiment was conducted to observe the grinding wheel motion and measure the grinding force. A computational fluid dynamics model was validated by particle imaging velocimetry to understand the flow field near the grinding wheel and estimate the hydraulic force. A grinding force model was established to describe the impact and cutting forces and experimentally validated.

The major achievements of this dissertation are:

(1) *The multi-grain grinding process simulation based on grinding wheel topography*: A grinding simulation using a grinding wheel with multiple abrasive grains and a workpiece with rough and realistic surface was carried out. The grain heights, shapes, and density in the grinding wheel model were from the wheel surface topography measurement. The workpiece surface geometry was generated by the measured abrasive geometry and grinding wheel kinematics. Grinding, of all the traditional machining processes, is the most challenging one to study, due to the multiplicity of the cutting points and their irregular geometry, the small depth of cut varying from grain to grain, and high cutting speed. Most grinding research either analyzes a single grain engagement with the workpiece or assesses the overall performance with

averaged grains. This presented multi-grain grinding simulation is able to show individual grain cutting, interaction between grains, and evolving depth of cut and workpiece surface during grinding, addressing both micro- and macro-cutting behavior of the abrasive grains.

(2) *A methodology to estimate the hydraulic force on the grinding wheel during atherectomy based on computational fluid dynamics modeling*: A computational fluid dynamics model was established based on the grinding wheel geometry and motion, validated by particle imaging velocimetry experiment, and used to estimate the hydraulic force on the grinding wheel. The grinding wheel in atherectomy rotates and orbits inside the artery at high speed. In this case, no direct method could possibly measure the hydraulic force on the grinding wheel without interfering its motion. This presented methodology solved this problem by calculating the force via a validated numerical model.

(3) *An experimental setup to investigate the high-speed intravascular grinding process in atherectomy*: An experimental setup with an arterial phantom, a high-speed camera, and a piezoelectric dynamometer was built for testing high-speed atherectomy grinding in an environment close to the human artery. Atherectomy in human artery is difficult to be characterized due to the inaccessibility and high grinding wheel rotational speed. The transparent soft PVC with designed elastic modulus and arterial phantom manufacturing technique allowed the visualization of the grinding wheel motion and interaction with the tissue-mimicking phantom. High sampling rate of the high-speed camera and dynamometer enabled the measurement of the high-speed grinding process. This setup could be exploit for testing other intravascular medical devices.

The original discoveries and key conclusions of this dissertation are:

(1) The rotating grinding wheel orbits around the vessel lumen during atherectomy. The grinding wheel rotational and orbital directions are the

same. The orbital speed increases with the rotational speed and the burr to artery ratio.

(2) The grinding wheel orbits at the orbital speed of 8,832, 9,210, 9,618, 9,930, and 10,248 rpm in a 4 mm lumen and 4,452, 4,638, 4,836, 5,052, and 5,262 rpm in the 6 mm lumen, while rotating at 135,000, 145,000, 155,000, 165,000, and 175,000 rpm, respectively, when a 2.38 mm burr is tested in a PVC arterial phantom.

(3) The grinding wheel orbital motion is caused by the rotation-induced blood flow near the grinding wheel. During orbiting, the hydraulic force on the grinding wheel is small comparing to the grinding force.

(4) The grinding wheel bounces on the wall of the calcified plaque while orbiting around the arterial lumen, leaving discrete grinding marks.

(5) In atherectomy grinding force, the bouncing grinding wheel impact force on the plaque is the dominant component. The cutting component for plaque removal is relatively small.

(6) The grinding force is 1.84, 1.92, and 2.22 N at 135,000, 155,000, and 175,000 rpm rotational speed, respectively, when a 2.38 mm diameter burr is tested in a bovine bone sample with a 4 mm lumen.

These findings facilitate to improve the atherectomy clinical guidelines and the device design. A grinding wheel smaller than the lesion lumen can remove the plaque due to its orbital motion, and the traditional clinical technique of increasing the grinding wheel size for removing more plaque may not be necessary. To reduce the atherectomy grinding force, lower rotational speed and smaller grinding wheel size and mass are suggested. Utilizing the grinding wheel orbital motion, new device can be designed to restore the patency of small, tortuous, and delicate luminal structures.

5.2 Future Work

The methodologies and models proposed in this dissertation could be further improved and extended in the following directions:

(1) Effect of the irregular lesion geometry on the grinding wheel motion and force can be characterized based on the presented experimental setup by developing arterial phantoms with patient specific lumen geometries.

(2) The presented plaque grinding study was based on the bovine bone surrogate to the calcified plaque. A more accurate model for the calcified plaque would give more insights in the plaque removal mechanism.

(3) Coupling the grinding force model and the computational fluid dynamics model by fluid-structure interaction study could provide better understanding of the atherectomy mechanism of action and clinical techniques.

(4) Debris formation and size distribution can be investigated by the presented multi-grain smoothed particle hydrodynamics grinding simulation which is critical to avoid down-stream embolism during atherectomy.

(5) Vessel dissection during atherectomy can be investigated with the presented grinding force model together with the vessel tissue mechanics.

(6) Current atherectomy device improvement or new device development can take advantage of the grinding wheel orbital motion and the impact grinding force modeling for more regular grinding wheel motion and controlled grinding force.

(7) The proposed multi-grain grinding simulation can be used in other grinding processes with various types of grinding wheel and workpiece.

APPENDIX I

As shown in Figure 4.9(b), O_w locates at (0,0), the workpiece profile is:

$$x^2 + y^2 = R^2 \tag{1}$$

Grinding wheel center, O_s locates at (0, $r - R$), and the grinding wheel profile is:

$$x^2 + (y - r + R)^2 = (r + f)^2 \tag{2}$$

Solving Eqs. (1) and (2) gives the intersection point **C** coordinates(C_x, C_y):

$$\begin{cases} C_x = \dfrac{\sqrt{4R^2f^2 + 8R^2rf - 4Rrf^2 - 8Rr^2f - 4r^2f^2 - 4rf^3 - f^4}}{2(R - r)} \\ C_y = \dfrac{-2R^2 + 2Rr + 2rf + f^2}{2(R - r)} \end{cases} \tag{3}$$

The arc angle, α, as indicated in Figure 4.9(b) can be calculated from (C_x, C_y):

$$\begin{aligned} \alpha &= \tan^{-1}\frac{C_x}{r - R - C_y} \\ &= \tan^{-1}\frac{\sqrt{4R^2f^2 + 8R^2rf - 4Rrf^2 - 8Rr^2f - 4r^2f^2 - 4rf^3 - f^4}}{2Rr - 2r^2 - 2rf - f^2} \end{aligned} \tag{4}$$

The contact arc length l_c can be computed as:

$$l_c = (r+f)\alpha$$
$$= (r+f)\tan^{-1}\frac{\sqrt{4R^2f^2+8R^2rf-4Rrf^2-8Rr^2f-4r^2f^2-4rf^3-f^4}}{2Rr-2r^2-2rf-f^2} \quad (5)$$